Reviewer 1 Responses

The study simulates a frontal rain band over the UK for which extensive radar and in-situ observations exist. Two new secondary production parameterizations are introduced to the COSMO model. The modeling is extensive in that it covers 16 sensitivities (+1 control) with 10 perturbations per configuration. These data are then used to compare to observations and assess the impact of the new parameterizations on ice number concentration and precipitation.

I think the study will be publishable after the following comments are addressed.

Thank you for your thorough reading and suggestions to improve it.

1/ My main issue is the experimental design (or my interpretation of it). To me, the problem is that the study appears to mix one secondary production process into the control model and then looks at the impact of the two new processes and modifications to the rime splintering process as 'the effect of secondary ice production...'. From what I can see in Table 2 there is no sensitivity with all secondary ice processes off. At the same time, the control model is stated as using Seifert and Beheng microphysics. The Seifert and Beheng described in the literature included rime splintering ice production. There are some comments later in the paper that suggest to me that the control does have rime splintering off. Therefore, either I have misinterpreted and some additional description of the control model configuration is needed, or I think we need an additional set of control runs that have no secondary ice production processes included.

Until there is a clean control with no secondary ice production processes it is difficult to interpret the statements about the impact of secondary ice production.

While we had not included the control run (CTRL) in the original version of Table 2, it was indeed done without any secondary ice production processes active; the default rime splintering of the Seifert and Beheng scheme was turned off. Thank you for pointing out that this was not explicit. In Section 3, we have rewritten: *A control simulation [is also run] in which all secondary ice production processes, including the default rime splintering in SB06, are turned off (denoted `CTRL' throughout).* We have also addressed some of the discussion of the CTRL versus non-control simulations below.

2/ The thrust of the paper is to show the impact of the different secondary ice production processes. Given the potential of introducing many unknown parameters into the model I think that it would be really useful for the community to try and identify if certain processes can be ignored. At the moment, the paper is pushing us to try to represent more complexity, but it would be advantageous if simplifications could be identified.

For instance, question that arise as I read through the paper include:

i. What is the relative impact of rime splintering to droplet shattering to collisional breakup? (Something similar was done for primary versus secondary)
ii. Can we ignore any of them or do they interact?
iii. Given the number of unknowns is it possible to write a single parameterization that captures all of the processes with less parameters? (this one would be speculation)

To try and answer i) and ii) the following families of model runs are suggested – some of which you already have.

a) Control: no secondary ice production (CTRL)
b) Control + rime splintering (RS1, RS2)
c) Control + rime splintering + droplet shattering (RS2+DS2)

d) Control + rime splintering + droplet shattering + collisional breakup (ALL)
e) Control + droplet shattering (DS1, DS2)
f) Control + droplet shattering + collisional breakup (DS2+BR2ig)
g) Control + collisional breakup (BR1ig, BR2ig, BR2sg)
h) Control + collisional breakup + rime splintering (RS2+BR2ig)

At both your and the other reviewer's suggestion, we have adjusted the study format. Some of the parameters used for rime splintering or droplet shattering were overly generous and results were not shown from several of the simulations in the first version of Table 2. We had also done no simulations with a single process, but rather with rime splintering *and* either drop shattering *or* breakup because part of our intent was to see feedbacks between these processes. In particular, we had been hoping to confirm or deny the existence of a kind of cascade effect (as proposed by Lawson et al. 2015) in which a few ice crystals formed from an initial droplet shatter or ice-ice collision then kick start rime splintering. To address the relative importance of the processes (your questions i and ii) for various thermodynamic regimes (your question iii in part and noted by the other reviewer), we have reorganized the simulations to be the following (summarized in a new Figure 2 and denoted above):

Rime splintering				**Ice-ice collisional breakup**			
RS1:	$\aleph_{RS} = 300,$	$w_{RS} = \text{TR}$		**BR1ig**:	*graupel_breakup_ice*		
					$F_{BR} = 180,$	$T_{min} = 256,$	$\gamma = 3$
RS2:	$\aleph_{RS} = 300,$	$w_{RS} = \text{UNI}$		**BR2ig**:	*graupel_breakup_ice*		
					$F_{BR} = 360,$	$T_{min} = 249,$	$\gamma = 5$
				BR2sg:	*graupel_breakup_snow*		
					$F_{BR} = 360,$	$T_{min} = 249,$	$\gamma = 5$
Droplet shattering				**Combinations**			
DS1:	$\aleph_{DS} = 2,$	$p_{max} = 5\%,$	$\sigma = 3$	**RS2 + BR2ig**:	$\aleph_{RS} = 300,$	$w_{RS} = \text{UNI}$	
					graupel_breakup_ice		
					$F_{BR} = 360,$	$T_{min} = 249,$	$\gamma = 5$
DS2:	$\aleph_{DS} = 10,$	$p_{max} = 10\%,$	$\sigma = 5$	**DS2 + BR2ig**:	$\aleph_{DS} = 10,$	$p_{max} = 10\%,$	$\sigma = 5$
					graupel_breakup_ice		
					$F_{BR} = 360,$	$T_{min} = 249,$	$\gamma = 5$
				RS2 + DS2:	$\aleph_{RS} = 300,$	$w_{RS} = \text{UNI}$	
Control					$\aleph_{DS} = 10,$	$p_{max} = 10\%,$	$\sigma = 5$
CTRL:	$\aleph_* = 0$	$F_{BR} = 0$		**ALL**:	$\aleph_{RS} = 300,$	$w_{RS} = \text{UNI}$	
					$F_{BR} = 360,$	$T_{min} = 249,$	$\gamma = 5$
					*graupel_breakup_**		
					$\aleph_{DS} = 10,$	$p_{max} = 10\%,$	$\sigma = 7$

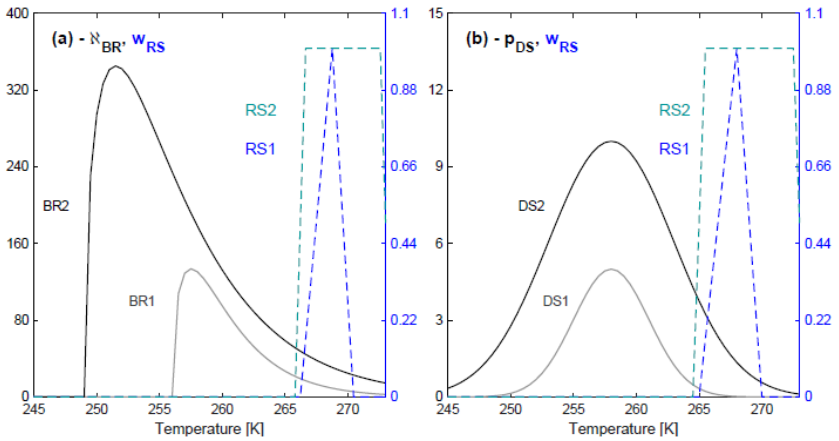

Figure 2 Fragment numbers, weightings, and probabilities from the secondary ice production parameterizations. In panel a, we show N_{BR} from both ice-ice collisional breakup simulations (BR1 and BR2) as well as the triangular and uniform w_{RS} (T). In panel b, we show p_{DS} from both droplet shattering simulations (DS1 and DS2) and w_{RS} once again.

To address your questions about relative importance and interaction, we have added a Figure 6 which compares the contributions from rime splintering, droplet shattering, collisional breakup, and all in combination in a 2 x 2 panel, as the old Figure 4 did for the primarily and secondarily formed ice crystal numbers.

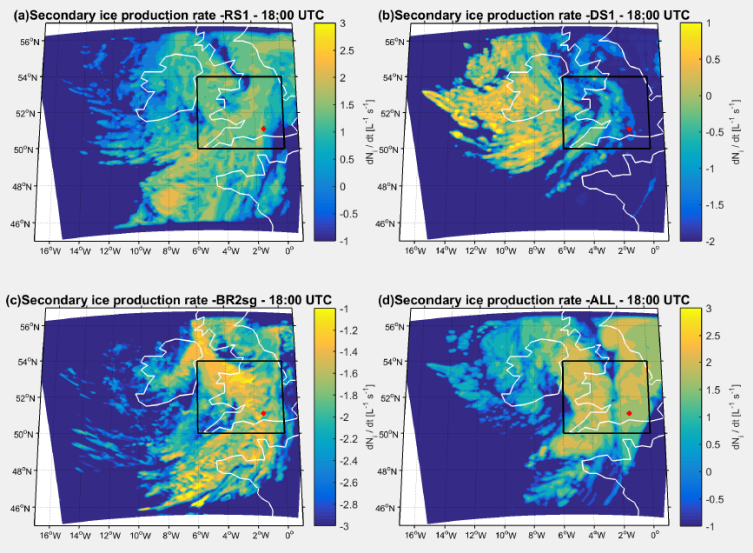

Figure 6 Maps to compare $N_{i,sec}$ between 18:00 UTC and 18:30 UTC from (a) rime splintering (RS1 at 3 km) (b) frozen drop shattering (DS1 at 4.5 km) (c) collisional breakup between snow and graupel (BR2sg at 1.5 km) and (d) all secondary processes occurring simultaneously (ALL at 4.5 km). Note the different logarithmic colorbars for each panel.

We have also added discussion of this to Section 4.2:

Next, we consider the relative ice crystal number concentrations produced by different processes in Figure 6. The largest $N_{i,sec}$ magnitudes, up to 1000 L^{-1} over the half hour, come from the RS1 and ALL simulations. These are followed by about 10 L^{-1} (half hour)$^{-1}$ generation rates from frozen droplet shattering and 0.1 L^{-1} (half hour)$^{-1}$ from collision breakup of snow and graupel. There is also an altitudinal hierarchy. Contributions from droplet shattering are largest at the highest altitudes of 4.5 km where raindrop number concentrations are still relatively high and the temperature (T in [237 K, 262 K] with a median of 249 K) is cold enough for non-negligible shattering probability. The rime splintering contribution is next at an altitude of 3 km, and the breakup is largest at a lower altitude of

1.5 km because the graupel mixing ratio is highest here. If graupel were present at higher altitudes, $N_{i,sec}$ from breakup could increase significantly, as both the snow mixing ratio and fragment number parameter increase at colder temperatures.

Finally, we have included fields of graupel and snow mixing ratios and rain drop number concentrations in the supplemental information, as well as a new section on dynamical intercomparisons – of wind speed, updrafts, and radar reflectivites – to make the discussion more thorough.

Additional points:

p. 5 eqn. 7. qrim is not defined. Is it the rate of change of ice due to riming?
q_{rim} is the rime mixing ratio. We add this to the description proceeding equation 7.

p. 6 table 2. SY not defined (typo on p. 5?)
We have eliminated the simulations that employed this symmetric temperature weighting for rime splintering (SY was for symmetric.)

p. 6, 13. CTRL = Seifert and Beheng – this has rime splintering secondary production as standard? [see main comment above]
You are right that in the default set-up Seifert and Beheng includes rime splintering. But we turn it off for our CTRL simulation and have made this clearer throughout the rewrite.

p. 8, 20. Maybe change secondarily -> secondary, primarily -> primary
We would prefer to leave the terminology as "secondarily-produced ICNC" / "primarily-nucleated ICNC" or "ICNC from secondary production" / "ICNC from primary nucleation".

p. 8, 28-29. Is COSMO able to capture this sort of mixing process?
We went ahead and removed this comment, as there is not extensive discussion of how COSMO represents vertical mixing in the model description.

p. 8, 30-p. 9, 3. 1Ag and 1Ac contain 2 changes. It's difficult to say which change is most important. Including 1An would provide a way to decide the relative importance of the changes.
Given the relatively large amount of observational evidence that suggests that the fragment number per milligram of rime should be on the order of 10^8, we have limited the rime splintering simulations to two with the standard triangular temperature weighting and a slightly extended one. So we will not discuss different fragment numbers.

p. 10, 7. 'There are no heating...' – do you mean because the structures are outside of the traditional temperature range for rime splintering?
We have moved this paragraph to the discussion section. The idea was that because rime splintering is a mechanical process, simply the shedding of fragile protuberances from rime, there is no latent heat release or consumption when it occurs. We have clarified: "*As mechanical processes, rime splintering and collisional breakup do not have direct latent heating effects.*"

p. 10, 8-10. 'Zhu et al...' I don't know if this can be inferred. I would imagine the melting differences affect the strength of downdrafts and cold pools leading to changes in subsequent convection which would be substantially different to the dynamical coupling due to latent heating in updrafts.
Yes, thank you. A more relevant study is that of Willison et al. 2013 *The importance of resolving mesoscale latent heating in the North Atlantic Storm Track* in which they discuss the latent heating effects on mid-latitude cyclogenesis and their spatial resolution dependence. We write:
Additional latent heating aloft can intensify the upper-level anticyclonic potential vorticity (PV) [Willison et al. 2013]. This PV generation may suppress further cyclogenesis by disconnecting the

developing system from surface potential temperature anomalies. On the other hand, additional cyclonic diabatic PV may slow system progression and maintain favorable levels of shear.

p. 10, 13-14. '...smaller droplets form, diminishing the riming...'. I think making smaller droplets could lead to increase cloud liquid water that would lead to increased riming.
Yes, this is true, but we were thinking of a case of fixed cloud LWC. In this case, more and smaller droplets should decrease the collisional efficiency between these and ice hydrometeors. We have made the fixed cloud LWC assumption explicit.

p.10, 16. Ni,sec – does this include all rime-splintering too? How does it compare to Ni,pri in a control model with no secondary ice production?
In the updated figure, $N_{i,sec}$ is indeed the secondary ice produced from rime splintering. Instead of showing its ratio relative to the primarily nucleated ice $N_{i,pri}$ we have chosen to show the absolute $N_{i,pri}$. This removes some numerical concerns (where one or the other tendency was absent and division created unrealistic values). Although we do not include it in the updated manuscript, here is an $N_{i,pri}$ field from the CTRL simulation:

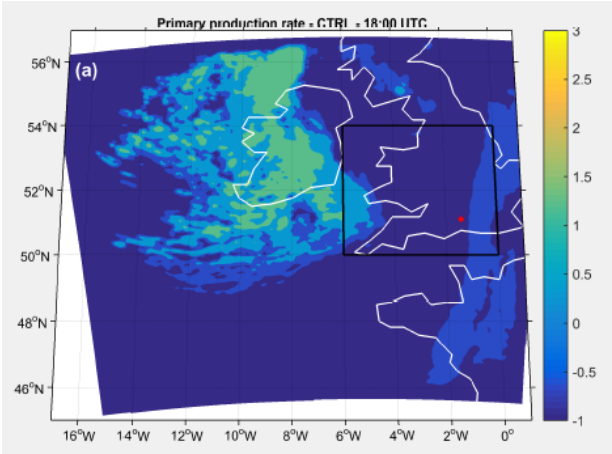

It has similar structure but somewhat smaller magnitude than the same field shown for the RS1 and RS2 fields in Figure 5.

p. 10, 27. This is a large domain that includes some of the warm front too?
Yes, this is true. It is the subdomain shown in black boxes in the new Figures 5 and 6, so an area that should also contain some of the warm front. We mention this in reference to some of the underestimation: *A final contribution to these too low ICNCs may be inclusion of parts of the warm front in the subdomain of analysis.*

p. 10, 30. '...filtered out'. These are in-cloud values then. Is it same thresholding for the observations?
The measurement accuracy does not extend to this low level, so we did not filter the observations in the same manner.

p. 11, 2. Control simulation – does this include rime splintering?
No, there is no secondary ice production in the control simulation.

p. 11, figure 4. How many points go into the 10^{-3} and lower probability for the observations? If it less than ~10 it might be good to ignore them?
We would prefer to keep the low-probability tail in Figure 7b to indicate the high degree of skewedness in the distribution. These instances, even if very few, are the ones most likely to reflect secondary ice production since N_{ice} is so high.

p. 12, 26. 'The control simulation without secondary ice...'. Is this the additional secondary ice processes or all secondary ice including rime splintering? If it is the latter then that needs to be made clear that the control has no secondary ice processes in it (see main point, p. 11,2, p. 6,13).
There is no secondary ice production in the control simulation. To remove confusion we delete "without secondary ice" here. In Section 3 on the Simulations, we write out: *"a control simulation in which all secondary ice production processes are turned off, including the default rime splintering in SB06 (denoted CTRL throughout)."*

p. 12, 32. How does figure 5 compare to observed accumulations?
The UK NIMROD radar data only offers rainfall rates. If we look instead at the CFARR ground site measurements of precipitation rate (Crosier et al. 2014 Figure 4b) we can very roughly integrate it. Say from 18:00 to 20:30 UTC there is a rate of 1.5 mm h^{-1} (= 4.5 mm) and another 1 mm h^{-1} from 21:00 to 22:00 (= 1 mm). If the rainband passage happens over a half hour with 60 mm h^{-1} intensity then we have a total accumulation of 4.5 + 1 + (0.5)(60) = 35.5 mm in the regions that saw the maximum precipitation intensity. This is not far off from the simulated values.

p. 13, 3. Please could you also give the domain mean precipitation change?
Yes, this is a good idea, thank you. We have written "*The sum of the deviations over the whole subdomain is an additional 23.9 m of precipitation for the RS1 simulation, 25.6 m for RS2, 16.9 m for DS1, and 16.6 m for ALL.*"

p. 13, 8. The red (positive) regions are also correlated with a combination of the location of the front and the orography, where convection may be enhanced.
Indeed. In reference to the location of the front, we write that *"Banding [in the P_{tot} deviations] reflects convective structure: vertical motion is strongest in the rainband leading edge, but also preceded and proceeded by downdrafts."* We have shown some of this dynamical structure in the new Figure 3c.

We had not considered the effect of orography; thank you for this suggestion. It could be that the particularly high P_{tot} seen in Figure 8a around 50.5°N and 4°W is due to orographic lifting by Dartmoor. We add the following description of topography to Section 4.3:
Orography in this region also has an impact. The spot of particularly large P_{tot} around 50.5°N and 4°W corresponds to the Dartmoor with a maximum elevation of 621 m. Slightly elevated P_{tot} is also present over the Exmoor and Bodmin Moor at (51°N, 3.5°W) and (50.5°N, 4.5°W).

p. 14, 4. The structures in Crosier et al are on the scale of ~5 km, whereas these are much bigger ~50 km?
Yes, you are right. A direct comparison of banded structure in the differential reflectivity and accumulated precipitation fields does not make total sense, so we have removed this particular comment. In general, however, we see "broadening behavior" in the simulations relative to the observations. For example, when we compare observed versus simulated radar reflectivity, we see that Z_{DH} values have a too-low magnitude over a too-great extent:

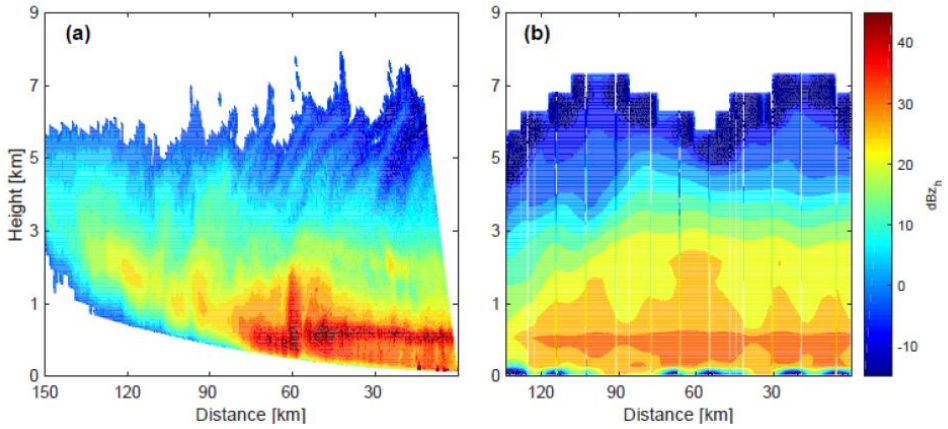

Figure 4 Model-measurement intercomparison of range-height indicator scans of radar reflectivity Z_{DH} along the 255 degree radial out from CFARR. CAMRa Doppler radar measurements are shown in panel a for the scan taken between 19:22:07 and 19:23:07 UTC, and modelare shown from the CTRL simulation at 19:00:00 UTC, both in dBZ_h.

Or in a qualitatively similar manner, we see too-low precipitation intensity magnitudes over too-great a time period in Figure 9.

p. 14, 9-11. 'suggesting that rime splintering is responsible for much of the change in P_{tot}.' Does this mean that the control did not have rime-splintering?
Yes, there is no secondary ice production in the control simulation. In Section 3 on the Simulations, we write out: *"a control simulation in which all secondary ice production processes are turned off, including the default rime splintering in SB06 (denoted CTRL throughout)."*

p. 14, 14. NCRF not defined?
Yes, thank you for pointing this out. We have added *narrow cold frontal rainbands (NCFRs).*

p. 14, 34. The variation in the means is now within 10% of the mean of the ensemble of results.
The differences in precipitation intensity vary less between simulations and deviate less from the CTRL simulation than those in precipitation accumulation. You are right that the difference in precipitation intensity from one simulation to another is not statistically significant. To the discussion in Section 4.3, we make explicit that "*In neither case does the evolution of the mean precipitation intensity for different simulations vary significantly from one to the next."*

p. 15, 1-6. Why not use the model to provide the diagnosed rates?
Yes, this is a good point. We opted to drop this analysis since it had significant numerical noise. Instead we have replaced these with temporal evolutions of the N_{ice} profile over time (in part to investigate the impact of seeding):

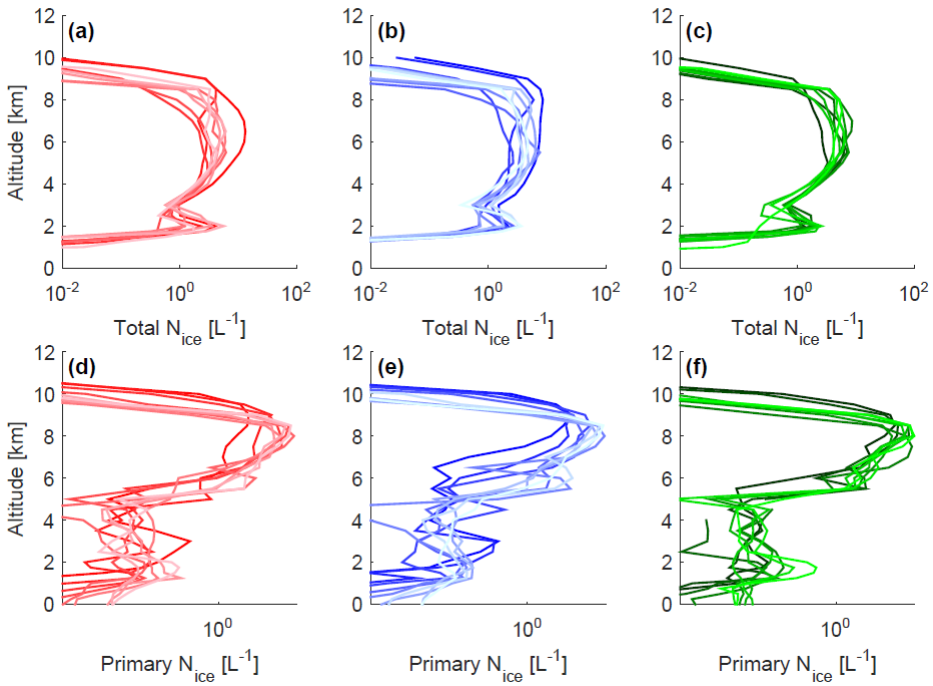

Figure S3 Temporal evolution of N_{ice} (panels a, b, c) and N_{pri} (panels d, e, f) profiles in the RS1 simulation from three, randomly-sampled latitude / longitude locations in the vicinty of CFARR. Eight profiles are shown for each location, one for each half hour from 18:00 UTC to 21:30 UTC with the darker colors representing earlier times and the lighter ones later times.

p. 17. It would be good to see answers to the points raised in 2/ above. It would also be good to state what the overall domain mean change in precipitation is due to secondary production processes.

We have added to the enumerated conclusions to address relative importance and parameterizability of these processes. To the first conclusion on ice production rates from primary nucleation versus secondary production, we build off the new Figure 6 and add:

"*In this case, we saw that rime splintering was the most important process in line with the conclusions of Crosier et al. 2014; however, underestimation of vertical velocities in the cold front also led to underestimation in simulated radar reflectivity relative to observations. If this Z_{DH} difference was caused by additional graupel at higher altitudes, contributions from collisional breakup could have been much higher than the 0.1 L^{-1} per half hour found here. A low bias in updrafts also generates fewer raindrops at altitude and limits the contribution from frozen droplet shattering (in this case to an intermediate production rate of 10 L^{-1} per half hour).*"

In regard to how the processes can best be parameterized we refer to the supplemental figure that shows large hydrometeor number concentrations or mixing ratios. There is a strong relation, for example, in the structure of the $N_{i,sec}$ from collisional breakup and the graupel mixing ratio. In the conclusions, we reiterate that: "*Underestimations stem in part from low biases in the updraft velocity. If the vertical velocities can be brought into agreement with observations, then criteria in these values as well as temperature could be used together to parameterize secondary production in appropriate thermodynamic zones. For two-moment schemes, graupel, snow, and raindrop criteria could be implemented for these processes.*"

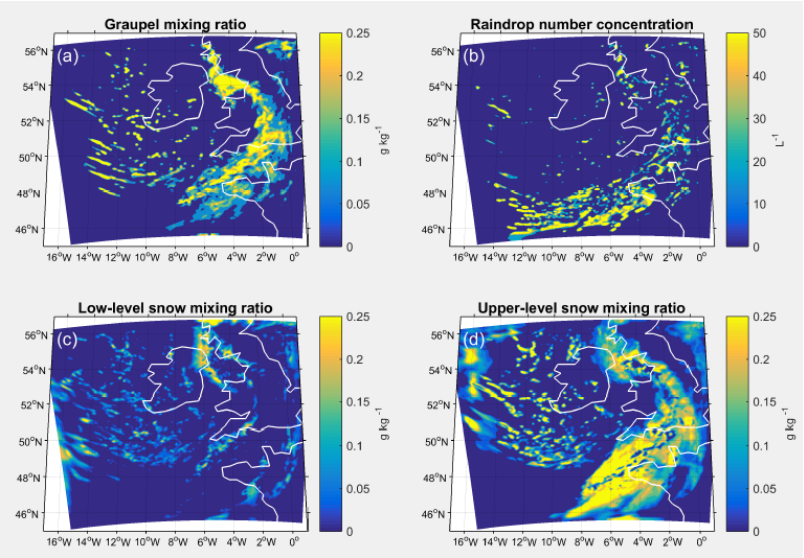

Figure S5 Graupel mixing ratio (a), snow mixing ratio (b), large-scale graupel quantity (c), and rain drop number concentration (d) in the simulation domain at 18:00 UTC for the RS2 simulation.

In regard to the second point, as mentioned in the response for p. 13, 3 above, we have written "*The sum of [P_{tot}] deviations over the whole subdomain is an additional 23.9 m of precipitation for the RS1 simulation, 25.6 m for RS2, 16.9 m for DS1, and 16.6 m for ALL.*"

Reviewer 2 Responses

General comments:

The authors conduct a numerical modeling study of secondary ice production and its possible effects on surface precipitation, based upon observations of the 3 March 2009 cold frontal passage across Southern England analyzed by Crosier et al. (2014). They address three kinds of secondary ice production: rime splintering, shattering of freezing raindrops, and collisional ice breakup, with several variations of coefficients that control the magnitude of each process. By enhancing the magnitudes of each process above that represented in past studies, or justified by laboratory experiments, they find (unsurprisingly) that the ice number concentrations can be greatly increased beyond that expected from primary nucleation. Through some (very rough) comparisons with the observations, they are still unable to replicate the maximum observed ice crystal number concentrations, and yet, estimates of the ice production rate actually exceed those based upon the observations. This disparity suggests that there might be some issues in comparing the observations and simulations, and/or that the simulated cloud dynamics are significantly different than in the observed clouds. The authors find an increase in surface precipitation of ~20% for the simulations that maximize secondary ice production, and advocate from that result that parameterizations of these processes should be included in large-scale models.

Thank you for your thorough reading of the work and suggestions to make it more rigorous. At both reviewers' behest, we have spent significant time to redo the simulations, adjust the structure of the study, and visualize new data from APPRAISE.

For the simulations, some of the parameter values that were chosen, particularly for rime splintering and droplet shattering were overly generous as you state. This was done, in part, to see if we were able to bring model and measured values into agreement with only modification to the secondary ice microphysics. Again as you state, we did not have agreement even at these extreme values, and so we have retained more conservative parameter values (sticking to, for example, 300 fragments (mg rime)$^{-1}$ for rime splintering) and modified the simulations as shown in the new Table 2 at the end of these responses.

Then we have added a section dedicated to reviewing the dynamical environment prior to any discussion of microphysical or precipitation (see responses to Comments 1, 6, and 8). This includes comparisons of radar reflectivity, updraft velocity, and surface wind speed.

Specific comments:

The authors are tackling a very difficult problem here, and studies like this are important and necessary. However, more care must be taken in what they can and cannot conclude from this study. I have some serious concerns with how the authors conducted some of the analyses, and/or their interpretations. In the manuscript, some very important details are omitted, that make it difficult to understand their interpretations.

Overall, I would like to see this study move forward, but feel that it would be of greater use to emphasize the temperature and dynamical regimes over which each of the secondary ice production processes is dominant, and how those differences assist (or do not) the formation of additional precipitation). That might be a more useful place to start when advocating that some of these processes be included in larger-scale models, as it would help focus case studies of the type of weather phenomena where they could have the most impact.

1. If observations and simulations are compared in this way, particularly when convective elements are contained within the weather phenomenon of interest, then it first must be demonstrated that the clouds and precipitation due to the cold frontal passage in the control case are consistent with that observed, and if not, to state clearly how they differ, and continue compensating for those differences when comparing the observed and simulated microphysical development. For example, a figure showing simulated radar echo can be produced, and shown alongside Crosier's Fig. 3 to understand how the general structure might differ. The timing is also important: if observations over a given time are averaged and compared with the simulations, any issues in doing so must be known. A small paragraph summarizing the dynamics of the observed clouds, based on the analysis of Crosier et al., would also be helpful in "setting the stage" for the reader, regarding the types of clouds (strengths of updraft speeds measured by aircraft, cloud top temperatures) being considered here.

Thank you for pointing out the need for these kinds of dynamical comparisons. We have compared modeled and observed radar reflectivity as you suggest. The comparison cannot be exact, as the field shown in Crosier et al. 2014 (and the CAMRa data in general) have much higher resolution along a radial whereas the model output exist only on the 2.8 km grid. In addition, the range-height indicator (RHI) of Crosier et al. 2014 comes from the CAMRa scan between 192207 and 192307 UTC, whereas we only have model output every 30 minutes.

Nevertheless, we calculate the latitude-longitude pairs along the 255° radial RHI in Fig 5b and identify the modeled lat-lon that minimize the Euclidean distance between these exact values and the model's spatial discretization. From here to generate an RHI, we iterate over a 1000 x 500 grid of distances and heights (relative to the Chilbolton Facility for Atmospheric and Radio Research) and do a bilinear interpolation over the nearest modeled lat-lons and 29 model levels to generate the radar reflectivities that are shown in the new Figure 4:

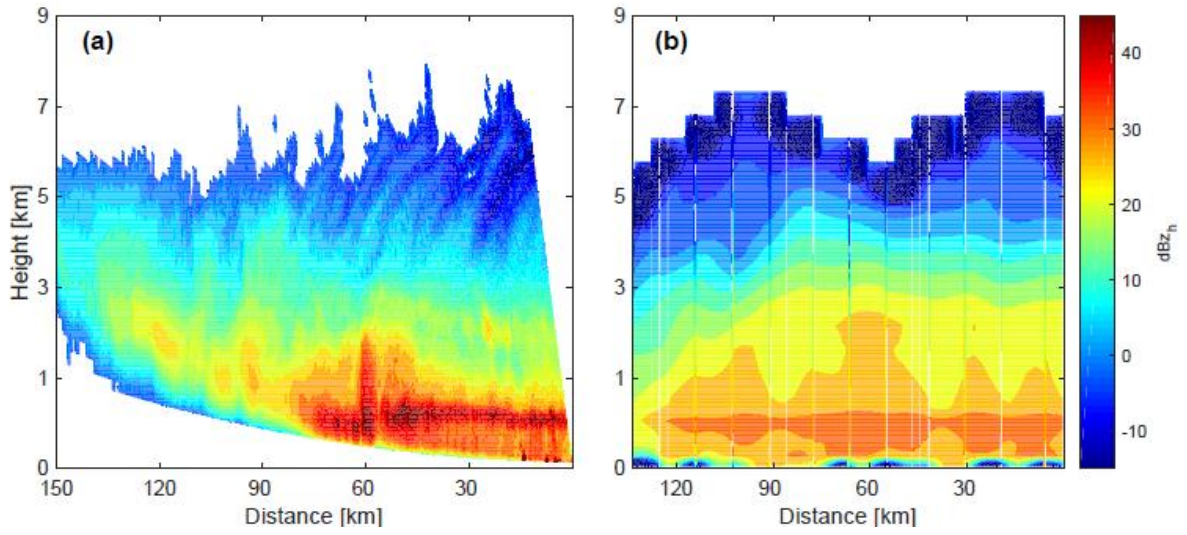

Figure 4 Model-measurement intercomparison of range-height indicator scans of radar reflectivity Z_{DH} along the 255 degree radial out from CFARR. CAMRa Doppler radar measurements are shown in panel a for the scan taken between 19:22:07 and 19:23:07 UTC, and modeled values are shown from the CTRL simulation at 19:00:00 UTC, both in dBZ_h.

We use the same methodology to calculate an RHI-type plot of the modeled updraft velocity; however this comparison includes an extra degree of inexactitude, as even the "observed field" is actually derived "using Doppler velocity measurements from RHIs by assuming mass-weighted flow continuity" [Crosier et al. 2014, Chapman and Browning 1998]. We have also compared modeled and observed (from the CFARR ground site) wind speeds and shown panels of modeled updraft velocity at two different altitudes during rain band passage in the new Figure 3:

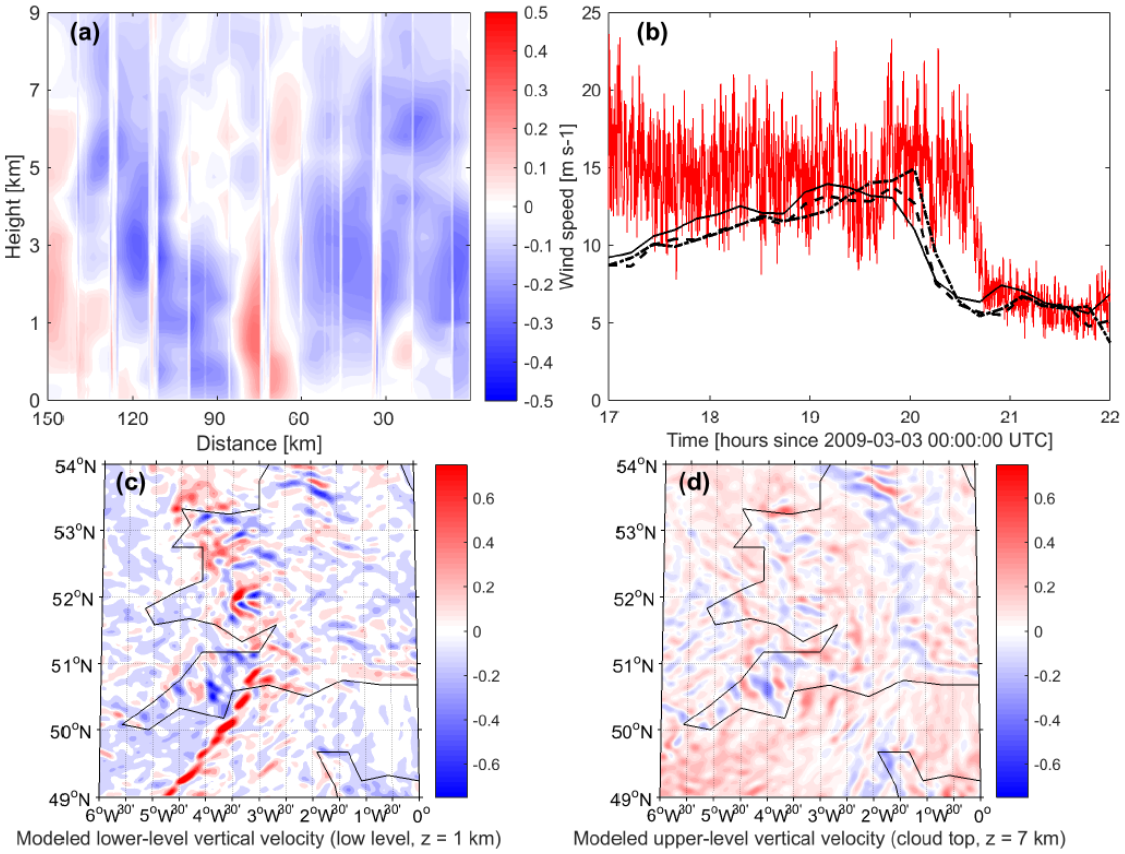

Figure 5 Different model dynamical fields. In panel a, we show the updraft velocity 150 km along the 255 degree radial from CFARR at 51.1N, 1.4W with values from the CTRL simulation at 19:00 UTC. Discontinuities are due to the minimization of Euclidean distance or interpolation aspects of an algorithm to approximate the radial from the model discretization. Surface wind speeds from 17:00 to 22:00 UTC from the CFARR three cup anemometer and our CTRL simulation are shown in panel b. Panels c and d show the modeled vertical velocities from the CTRL simulation at 1 and 7 km respectively at 18:00 UTC as the rainband began to pass over the UK.

We describe these methods and comment on their impact on microphysical comparisons in a new Section 4.1 on the *Dynamic environment*:

4.1 Dynamic environment

We begin by comparing the observed and modeled dynamics to understand how these differences may impact later microphysical ones. We show the updraft along a 255° radial out from the CFARR station (Figure 3a) as in Figure 5d of Crosier et al. 2014. Comparison to simulations cannot be exact, as the output from the model exists along a coarser spatiotemporal grid. We use those w values whose latitude-longitude pair minimizes the Euclidean distance to the precise values along the radial. Thereafter we interpolate both over distance and altitude on a 1000 x 500 grid to generate the range-height indicator (RHI)-type plot. This interpolation leads both to intermittent discontinuities and to weakening of extremes. The upright updraft region about 60 km from CFARR appears distinctly in the simulated field but with vertical velocity magnitude far smaller but extent far greater than those derived from measurements (maximum of about 1 m s^{-1} relative to about 6 m s^{-1}). Downdrafts of more similar magnitude and extent to those observed also form in adjacent regions. Values derived from Doppler velocities (v_u) also rely on an assumption that at low elevation, v_u approximates the horizontal wind and that any convergence or divergence of these horizontal winds within discrete columns must conserve mass with a compensating upward or downward velocity.

Comparison of the surface wind speed both in the CTRL simulation and from a three cup anemometer at CFARR is also shown in Figure 3b. Three series are shown from the simulation at latitude and longitudes closest to the center. Simulated wind speed peaks too early but to a value only slightly less than the average of the observations. Both series display a sudden drop in the strength of these winds with similar decay rates and plateau

values of about 5 m s^{-1}. Perhaps most important is the consistent underestimation of these surface winds prior to the rainband event, from 1700 to 1900 UTC. Given that the direction of low-level winds preceding the rainfall event was southwesterly (Crosier et al. 2014, their Figure 4b), underestimating their magnitude will diminish the oceanic moisture advection and moisture source ultimately available to form rain over the continent.

Figures 3c and d also show the vertical velocities in the CTRL simulation at altitudes of 1 and 7 km at 1800 UTC as the rainband reaches land. Its structure is apparent in the low-level updrafts of about 1 to 2 m s^{-1} (although these are again much weaker than those from observations) and their adjacent downdrafts with similar magnitudes of opposite signs. Elsewhere values are ± 0.2 m s^{-1} with slow descent presiding. For the upper-level field that corresponds to cloud top, the highest ascending motions also occur around the rainband region and slow ascent (≤ 0.4 m s^{-1}) dominates.

We next compare range-height indicator (RHI) scans of radar reflectivity (Z_{DR}) from the Chilbolton Advanced Meteorological Radar (CAMRa) and the CTRL simulation (Fig.4). The CAMRa is a 3 GHz Doppler instrument with a 0.28° beam, and its scan between 192207 and 192307 UTC along the 255° radial out from CFARR is shown, as in Figure 5a of Crosier et al. 2014. We use output from 190000 UTC in the CTRL simulation and again identify the modeled latitude-longitude pair that minimizes the Euclidean distance to the exact value from along the 255° radial. We then perform bilinear interpolation on the simulated values of Z_{DR} over a 1000 distance x 500 altitude grid.

The CAMRa scan shows the location of cloud top height and convective activity: the lowest Z_{DH} is around 6 to 8 km and fall streaks are present moving toward the CAMRa. These Z_{DH} fall streaks, as well as those in differential reflectivity (shown in Crosier et al. 2014 their Fig. 5c) indicate that ice crystal seeding may be occurring near cloud top. Intermediate values of Z_{DH} occur at altitudes of 2 to 5 km, and the highest ones occur around the melting layer at 1 to 2 km, as discussed by Crosier et al. 2014. General features are replicated in the simulated reflectivities. Very low Z_{DH} occur close to CFARR with cloud top around 7 km, but further out -- around 70 to 100 km along the radial -- these same very low reflecitivities occur more often than in the measurements. The gradient to higher Z_{DH} at lower altitudes is also apparent in simulations, but not as distinct fall streak structures. Z_{DH} has increased to about 10 dBZ_h by a height of 4 km and about 20 dBZ_h by a height of 2 km. The highest reflectivities also fall in the same altitudinal range, but importantly do not have the same maximum as in the observations. Z_{DH} in an updraft core 60 km from CFARR reaches a value of 45 dBZ_h in the CAMRa but only 30 dBZ_h in the CTRL simulation. This may be due to underestimation of graupel formation or too high CCN or INP concentrations that delay precipitation in the base COSMO model [e.g., Baldauf et al. 2011]. We keep this underestimation in mind in the proceeding discussion of microphysical adjustements.

2. The routes from ice to precipitation discussed in the introduction, shown in Fig. 1, and later discussed with respect to effects of the secondary ice upon precipitation, are not inclusive of a major route from ice crystals to precipitation: enhanced rimed ice / rimed snow / graupel / frozen raindrop formation that can melt to become surface precipitation. In Fig. 1, it is somewhat suggested by (3), but the arrow isn't drawn as leading to acceleration of precipitation like (2). Such an analysis of that route to precipitation is completely omitted in the manuscript. Why?

   Thank you for pointing out this missing mechanism. Figure 1 focused on showing how secondary ice production (solely) impacts precipitation via increased ice crystal number concentrations, so we had not included impacts of just riming (only rime splintering). But we agree that a more complete analysis cannot consider secondary ice processes in isolation, and we have added enhancement of precipitation by rimed hydrometeors to the schematic. To the discussion of cloud ice-precipitation linkages, we add the following:

   Efficient riming at mixed-phase temperatures may also simply generate larger hydrometeors that sediment more quickly, particularly in convective regions with a high degree of mixing.

   Even if no graupel were observed, the Crosier et al. paper discussed the importance of rimed snow, and noted that the aircraft did not sample the stronger convection where graupel might have resided. The authors only discuss in this study the possible effects on the Bergeron process leading to precipitation, but that would be more important in the stratiform precipitation regions, and not as

much in the convective regions of the cold front band, where the heaviest precipitation will fall. I would think that the precipitation enhancement see in Fig. 5 is due to rimed particles, not from an enhanced Bergeron process.

Elsewhere in the introduction, we note that *in cases of ice-initiated precipitation, the requisite crystal growth can occur **via riming** or the Bergeron process.* In the discussion of ice-precipitation linkages, we note that *this pathway [of small crystal formation depleting supersaturation until the Bergeron process initiates] should be more important for stratiform precipitation, given the narrow range of requisite ambient vapor pressures: indeed for an integral ice radius of 100 um cm^{-3}, the updraft must be less than about a 1 m s^{-1} for the Bergeron process to occur [Korolev 2007].* To the discussion of impacts on precipitation, we add that *this amplification may be due in part to more riming in the ascending regions, which feeds into precipitation both directly as rimed particles sediment and melt (Fig. 1(3)) and indirectly as they splinter and generate more rimable particles (Fig. 1(4)). Crosier et al. 2014 note that higher values of differential reflectivity around cloud top could be due to high concentrations of rime particles.*

3. The implementation of the secondary ice parameterizations in the two-moment Seifert and Beheng scheme are confusing.

a. Why is the second moment not taken advantage of here? Everything seems to depend upon mass.

We are indeed taking advantage of the second moment outside of the fragment number parameters. Within the ice-ice collisional breakup formulation for example, the D_j and D_k in Equation 6 are the particle diameters associated with particle mass through a power law as detailed in Appendix B. Within the droplet shattering formulation, the tendency of freezing droplets in time is a function of the mean mass per raindrop as detailed in Appendix A.

The importance of the second moment extends beyond a collision or freezing tendency to the fragment number parameters, and you are right that this dependency has not yet been incorporated. There is not enough consensus of laboratory and in-situ measurements to support one fragment number function in our opinion. We expand the section on the frozen droplet shattering parameterization (Section 2.1) and add to our comment in the earlier version that *future studies should add dependency on droplet size to the ejected fragment number*:

Recent droplet levitation experiments and high speed video are elucidating the exact physics behind the shattering of droplets as they freeze [Leisner et al. 2014, Wildeman et al. 2017]. Droplet shattering has been previously parameterized statistically in a bin microphysics scheme with the fragment number as a function of drop diameter to the fourth power, using data from the Ice in Clouds Experiment - Tropical (ICE-T) campaign [Lawson et al. 2015, Lawson et al. 2017]. But while measurements continue to confirm a strong dependence of fragment number on droplet size, even recent studies could not confirm this fourth-power dependence [e.g., Lauber et al. 2018]. The laboratory studies of Lauber et al. 2018 in particular add important quantitative results to existing secondary ice measurements but are taken at two droplet sizes (83 and 310 um) so that it remains difficult to rigorously formulate fragment number.

To the section on the ice-ice collisional breakup parameterization (Section 2.2), we also add discussion of other parameterizations:

Vardiman first parameterized ice-ice collisional breakup using fragment generation functions based on the momentum exchange between two particles upon impact and leading coefficients dependent upon crystal type [Vardiman78]. More recently, Yano and Phillips 2011 and Yano et al. 2016 constructed a dynamical system-type models that tracks only ice crystal, small graupel, and large graupel number densities and illustrated the ability of ice-ice collisions to generate huge ice crystal enhancements in the absence of vapor limitation. Recently a more complete parameterization has used an exponential formulation with the initial kinetic energy of two particles, their temperature- and humidity-dependent collision type, and asperity fragility coefficients [Phillips 2017a, Phillips 2017b].

We choose to focus on temperature dependence in a more straightforward, if less physically rigorous, product of fragment number and hydrometeor collision tendency.

For example, rime-splintering appears to have a constraint of rimed mass, but for a two-moment scheme, the Cotton et al. (1986) second formulation that uses the number of fragments per number of 25 um diameter drops accreted would be a better prediction. The lab studies have shown that if the rimed drops don't achieve this size they won't splinter. As implemented here, there is no drop size dependence, so splintering might be greatly overestimated, and some commentary needs to be given in regards to that limitation.

In connection with the previous comment, this statement is a bit confusing, as it advocates for use of the first moment *rather* than the second moment. Nevertheless, we had made the rime splintering parameterization active only for rain drops. At the end of Section 2.3, we had stated: *We limit rime splintering to occur only after collisions between raindrops and ice crystals, graupel, or hail.* However, raindrops in the Seifert and Beheng scheme have a radius of 40 um, and as you state, the radius of onset for rime splintering is lower, around 12 um. So we have gone back and implemented rime splintering with cloud droplets as well, defining a 12 um threshold radius for these cases. We adjust the Section 2.3 description:

We also limit rime splintering to occur only after collisions between cloud droplets of diameter greater than 25 um or raindrops (r > 40 um) and ice crystals, graupel, hail, or snow [e.g., Phillips et al. 2001, Connolly et al. 2006b].

b. Along similar lines, what is the justification for the experiments using broader temperature ranges and/or increased fragment numbers for rime splintering? That process has been studied much more in the laboratory than others (Hallet and Mossop and Saunders & Hosseini, AR, 2001). The results here seem to rely on the expansion of this process to a broader area of temperature than appears justified by the laboratory work. The latter study also looks at the importance of fall speed, where graupel is more favored for greater splinter production. Since the simulation has little / no graupel here, then it would seem to imply using smaller splintering rates is appropriate.

Some justification comes from the potential dependence of the process on rimer surface temperature rather than ambient temperature [Heymsfield and Mossop, 1985], but not to the extent that our initial rime splintering temperature weightings (w_{RS}) reached. We have amended w_{RS} to the typical triangular weighting between -3 and -8°C and a uniform one between 0 and 10°C. The latter is still somewhat generous in order to pick up on any potential "cascade effect" between a droplet shattering or ice-ice collisional breakup "trigger" and rime splintering. We note this specifically in Section 2.3:

We add a second, uniform temperature weighting (UNI) between 263 and 273 K to investigate the possibility of a droplet shattering or ice-ice collisional breakup `trigger' that feeds into a rime splintering `cascade'. The rimer surface temperature may in fact be the more important factor and can remain between 265 and 270 K, even for cloud temperatures a few degrees colder [Heymsfield 1984].

c. Also, there is no mention of the recent work on ice-ice collisions, and its parameterization by Phillips et al. (Phillips et al., JAS, 2017 and 2017) or for shattering of freezing drops ((Phillips et al., JAS, 2018). How do their parameterizations compare to those used here, and how might that influence differences in the effects upon precipitation?

Thank you for pointing out this oversight. As noted above (in response to point 3a), we have noted the existing breakup parameterizations in an expanded Section 2.2. To the end of this section, we note the differences in the importance of temperature, as our formulation depends directly and solely on temperature: *We expect a strong influence of temperature from our breakup tendency* $(\delta N_{ice}/\delta t)_{BR}$ *than was discussed in Phillips et al. 2017b, given the direct and sole dependence in Equation 5.*

4. It is stated that Crosier et al. noted fall streaks at cloud top in the radar measurements. This would seem to imply a seeding mechanism of ice from above that could also have fallen to the observation level of the aircraft, unless this has somehow been ruled out?

Thank you for this suggestion. Generally, an $N_{i,pri}$ peak at an altitude and an N_{ice} peak at a slightly lower altitudinal band should be a signature of seeding. The new Figure 7 (old Figure 4) could address this somewhat, but to be more thorough we have included two supplemental figures that show the vertical profiles of N_{ice} and $N_{i,pri}$ over time. For example, three locations near CFARR are shown in panels a, b, and c here with the darker colors corresponding to earlier times and lighter ones to later times:

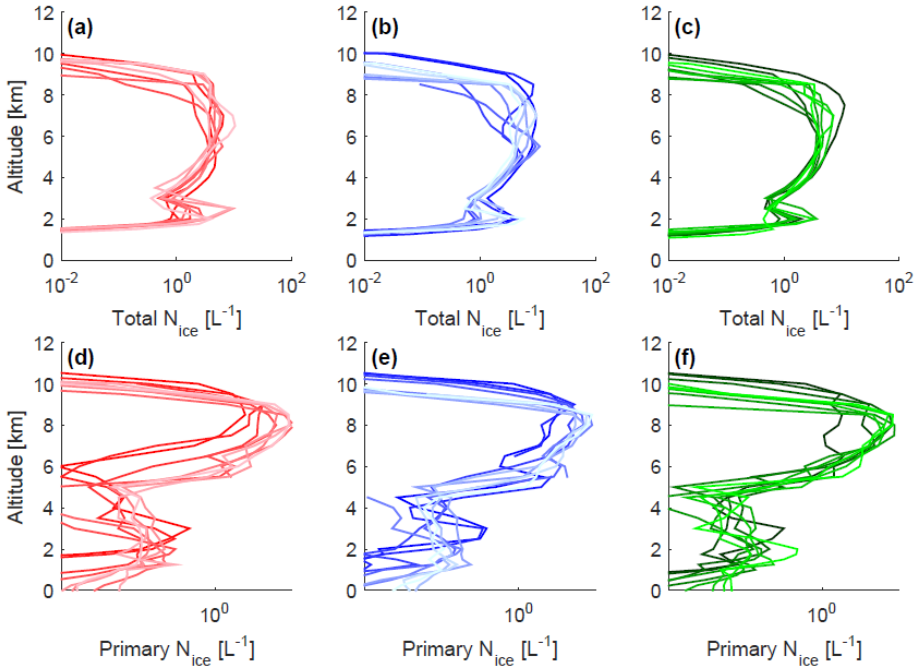

Figure S3 Temporal evolution of N_{ice} (panels a, b, c) and $N_{i,pri}$ (panels d, e, f) profiles in the RS1 simulation from three, randomly-sampled latitude / longitude locations in the vicinty of CFARR. Eight profiles are shown for each location, one for each half hour from 18:00 UTC to 21:30 UTC with the darker colors representing earlier times and the lighter ones later times.

Around cloud top, we do see that the peak in N_{ice} extends below that in $N_{i,pri}$, but these temperatures are too cold for droplets to exist, so this should just be the signature of ice sedimentation. There are secondary peaks in both N_{ice} and $N_{i,pri}$ at lower altitude, but both also exhibit a "pinch point" above this, i.e. there is not consistently a nucleation source about the low-level N_{ice} peak. This low-level peak should mostly be due to secondary ice production.

We summarize this by stating the following in the new section on the Dynamic environment: "*these Z_{DH} fall streaks, as well as those in differential reflectivity (shown in Crosier et al. 2014, their Fig. 5c) are signatures of ice crystal sedimentation and aggregation near cloud top. Ice crystal seeding may also be occurring with lower-level sedimentation, but the altitudinal peak in $N_{i,pri}$ does not fall consistently above that in N_{ice} (Figs. S3 and S4) so that secondary ice production must generate a portion of this low-level ice.*"

5. I would contend that most "larger-scale models" do not have two-moment microphysical schemes, so that the suggestion at lines 21-24 on page 10 are not practical.

Yes, you are right; within the CMIP5 models, the majority still use single-moment cloud microphysics schemes. But two-moment schemes generally lead to better representation of factors like greenhouse gas warming trends, snowfall intensity, and stratiform precipitation extent [Ekman 2014, Molthan and

Colle 2012, Morrison et al. 2009]. The IPCC has summarized its Fifth Assessment Report by saying that "climate models are incorporating more of the relevant aerosol-cloud interaction processes than at the time of AR4, but confidence in the representation of these processes remains weak." We take these results and trends to indicate that future model development will favor the incorporation of two-moment schemes. Indeed, given the uncertainties still associated with secondary ice production parameterizations, their model inclusion should generally come after the shift to a two-moment scheme.

Nevertheless we qualify our recommendation and note, as you mention above, that it may be more helpful initially to identify thermodynamic regimes under which these processes need to be included:

As meso- and large-scale models transition toward two-moment cloud schemes, secondary ice production could be included in parameterizations with criteria for the number concentration of large hydrometeors: the droplet shattering and collisional breakup parameterizations are activated only for those cloudy grid cells with more than a threshold concentration of large droplets and graupel, hail, or snow respectively. In one-moment schemes, parameterizations on the basis of favorable thermodynamic regimes will be more useful for the time being.

6. Comparison of observations and modeling: unless the authors can justify that the simulated movement of the rainband, and its dynamical nature, was very similar to that observed, it would make the comparisons shown in Fig. 4 not very useful. (If the comparison is not "fair", it could even be the case that the model IS producing sufficient secondary ice, for example, if the dynamical / thermodynamical conditions of the simulated clouds in that region and over that time are different than observed!) The description of the analysis for panels b and c on page 12 is helpful, but the reader cannot see what is being compared (which is why some comparison of the observed radar evolution to the simulated one is needed early on in the paper.) The temperature ranges also need to be specified in Fig. 4, too.

This is an important and difficult point that you raise again. We have provided a description of the simulated dynamics in our response to your first comment and see that the embedded updrafts, the preceding surface winds, and the reflectivities within the rainband are all weaker than in the observations. But it is also the case that the old Figure 4 (now Figure 6) intended to show how important the secondary production is relative to primary nucleation in the model. We were considering the simulated fields only because there is no way to make an analogous comparison with the available data. However, we still note in the rewritten discussion that "*underestimation of the updrafts within the rain band core (Sec. 4.1) will lead to errors that offset each other somewhat: too few raindrops will form when the vertical velocity and supersaturation are too low, but these will also be lofted more quickly through the altitudinal band where rime splintering is favoarble, leaving less time for collisions to occur.*"

In general, this kind of "dynamical buffering" for secondary ice production (i.e. that they require large hydrometeors but that also sufficient time in an appropriate temperature zone) should give some "dynamical resilience" to the simulations. In discussion of the altitudinal profiles of N_i, we also point out that "*The underestimated updrafts and radar reflectivities noted above in Section 4.1 may also help explain the too low N_i around 2 km: larger vertical velocities could loft graupel to high altitudes and boost the contribution from collisional breakup.*

To aid with visualization of what is shown in the new Figure 7 (altitudinal profile, histogram, and time series of N_{ice}), we have made the outline of the subdomain surrounding CFARR more prominent in Figures 5 and 6 and mentioned explicitly that we are drawing from this subdomain in the figure caption.

We have also switched Figure 6 to an altitudinal slice rather than a pressure level. We indicate in the caption now that "*The median temperature at this altitude is 255 K with a minimum value of 245 K and a maximum value of 267 K*."

7. Ice production rates: it needs to be stated more clearly how these derived from both the observations and the modeling results. Right now, it is unconvincing that this comparison is valid. Also, it should be stated somewhere that the CIP-15 observations were corrected using an algorithm designed to remove shattering artifacts, but some still likely remain because anti-shattering tips were not used on the instrument, as stated by Crosier et al.

   Yes, thank you for pointing out that the details of this calculation were missing. We had used a centered finite difference:

$$\left.\frac{dN_{ice}}{dt}\right|_{t_i} = \frac{N_{ice}\,(t_{i+1}) - N_i(t_{i-1})}{t_{i+1} - t_{i-1}}$$

   But we agree that this analysis is not as informative as focusing on the temperature-dynamic regimes where ice production is largest. For that reason, we remove the ice production rate figure.

   Within what is now Section 4.2 on Ice production rates, we also describe the CIP-15 measurements more thoroughly:

   IAT algorithms, with those particles below a threshold IAT of 10^{-4} s classified as artifacts, were used to correct the ICNCs [Field et al. 2006b]. No shatter-resistant tips were used on the probe, but given the strict IAT threshold, the possibility of artifacts is limited.

8. Qualifiers / limitations: need to be stated clearly throughout the paper. For example:

a. The model uses the primary ice nucleation parameterization of Phillips et al. (2008). Since INP measurements were not collected, it is unknown if this is an accurate representation, or not, and this might greatly affect the ratios of secondary to primary nucleated ice, including the possible importance of secondary ice to precipitation.

   Yes, this is a good point to include. In Section 3 on the Simulation setup, we add

   Previous studies have noted that limited nucleating efficiencies in the PDA08 may lead to underestimation of ICNC at mixed-phase conditions [Barahona et al. 2010, Curry and Khvorostyanov 2012, Morales-Betancourt et al. 2012]. No ice nucleating particle (INP) measurements were made during this case study, but from other observational datasets, PDA08 still yields better agreement with in-situ ICNCs than purely lab-based or theoretical parameterizations [Sullivan et al. 2015].

   Here it is also important to point out that Crosier et al. have noted the potential for large contributions of homogeneous nucleation in the convective regions. We point out right after the comment above that

   Crosier et al. also note that the low cloud top temperatures and strong updrafts in convective regions generate supersaturations that could favor large ice production from homogeneous nucleation. While not observationally confirmed, these conditions could buffer the ice nucleation tendency to our choice of parameterization.

   In what is now Section 4.2 on ice production, we also add the following caveat:

   The magnitude of these values is subject to uncertainty from the nucleation parameterization, which, as noted above, has underestimated INP numbers in previous studies.

b. To show an appreciable effect on surface precipitation (20% increase), rime splintering had to be increase over that typically depicted in models based on the laboratory measurements (e.g. Cotton et al. 1986 parameterization).

We have only left one test with an extended rime splintering where rime splintering is permitted to happen for 2 K below the typical threshold of -8°C. Earlier we had also made the error of showing the precipitation accumulation at 18:00 UTC ("as the rainband begins to pass over the UK" stated in the caption). We now look at the accumulation from the final model output file (23:30 UTC) after complete rainband passage and see accumulation differences on the order of 10 mm. Precipitation intensity differences remain about ±5 mm h^{-1} for a maximum simulated intensity of 30 mm h^{-1} (the 20% you cite) for the adjusted simulations.

c. Reasons for why the other two secondary ice processes might be less important here: (i) minimal graupel, which is important for ice-ice collisional breakup; (ii) limited number of raindrops? (Not sure what else would have limited that process here, but it would be good to know.) Also, it should be explained that the Crosier et al. study noted limited graupel in their observations, and I don't think they found any evidence of shattered frozen raindrops, but they clearly state that the former could have been limited by the inability of the aircraft to fly in the more convective regions.
Thank you for your thoughts. Building off these, we have included the spatial fields of graupel and snow mixing ratios and rain drop number concentrations in a new supplemental Figure:

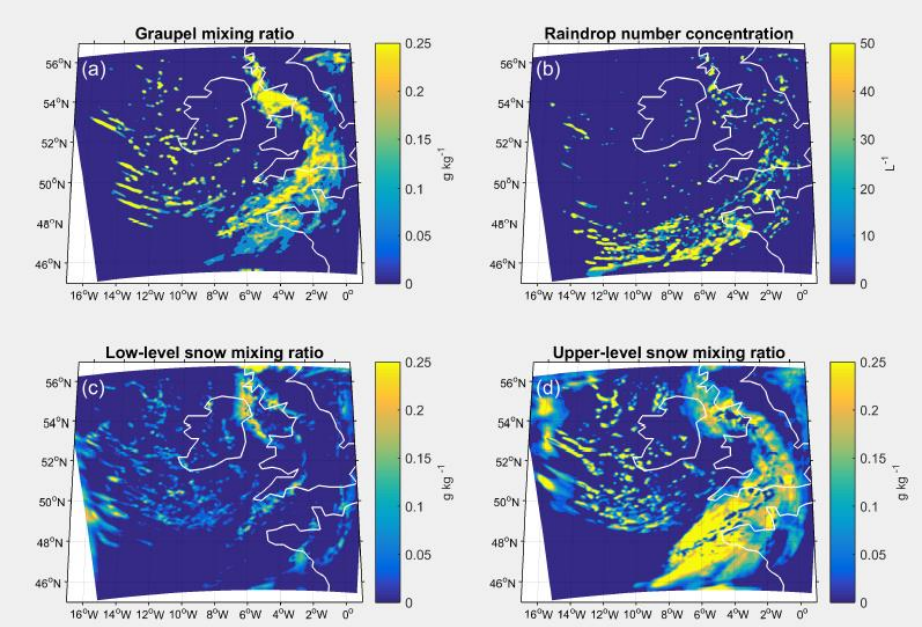

Figure S5 Graupel mixing ratio (a), snow mixing ratio (b), large-scale graupel quantity (c), and rain drop number concentration (d) in the simulation domain at 18:00 UTC for the RS2 simulation.

From these, we agree that low graupel and raindrop concentrations at the appropriate altitudes are limiting the $N_{i,sec}$ from collisional breakup and droplet freezing. To Section 4.2 we add the following:
If graupel were present at higher altitudes, $N_{i,sec}$ from breakup could increase significantly, as both the snow mixing ratio and fragment number parameter increase at colder temperatures. Similarly very limited raindrop number concentrations exist at the altitude where shattering probability is non-negligible. This importance of large hydrometeor number concentration for $N_{i,sec}$ suggests a means of parameterizing secondary ice production as meso- and large-scale models transition toward two-moment cloud schemes: the droplet shattering and collisional breakup parameterizations could be activated only for those cloudy grid cells with more than a threshold concentration of large droplets and graupel, hail, or snow respectively. In one-moment schemes, parameterizations on the basis of favorable thermodynamic regimes will be more useful for the time being.

d. The enhancement of the updrafts and precipitation, and downdrafts, mentioned on page 14 needs to be backed up with some evidence.

We have deleted this statement because we are not showing a feedback of the ice production on dynamics yet. With the updraft field in the new Figure 3 we can only state that the regions of highest precipitation intensity (and precipitation intensity deviation) occur in the regions of highest vertical velocity.

e. Some discussion of the model resolution effects should be included, for both properly simulating the microphysics as well as the dynamics.
Within the discussion section, we have added discussion on the potential impact of resolution and the particular microphysics scheme on our results:

The choices of spatiotemporal resolution and microphysics scheme are particularly important for convective clouds because of the fine structure of precipitation and strong feedbacks between hydrometeor formation, latent heating, and cloud dynamics. Previous studies have generally found a spatial resolution of 4 to 6 km to be sufficient to reproduce precipitation extremes [e.g., Prein et al. 2013, Pieri et al. 2015]. This resolution dependence results from changes in the vertical moisture advection, in turn due to adjustments of vertical velocity with resolution [Yang et al. 2014]. For simulations whose resolutions border on the ``gray zone" scales (around a tenth of a degree), over-representation of convective activity is possible by both the parameterization and explicit resolution [Pieri 2015]; however, our simulations are at a fully convection-permitting scale and use only a reduced form of the Tiedtke mass-flux scheme for shallow convection [Tiedtke 1989] and this should not be a concern.

The use of a two-moment scheme is also important for simulation of extreme precipitation [Otkin 2006]. Certain one-moment schemes tend to generate overly large drops and too high precipitation rates [Thompson 2004], but SB06 tends to produce especially large quantities of graupel [Otkin et al. 2006]. The Bigg parameterization, as a precursor to our droplet shattering additions, has been shown in previous studies to predict very low numbers of frozen drops [e.g., Morrison et al. 2005, Fan et al. 2009], which may contribute to underestimate of secondary ice here. The more rigorous alternative would be to account for immersed surface area and scavenging of ice nucleating particles as in [Paukert and Hoose 2014, Paukert et al. 2017], and future work should implement both an updated immersion freezing and secondary ice parameterizations.

Technical Corrections:

1. Table 2 and Fig 2 are confusing, since most of these runs are not discussed in the paper. I would suggest only showing those that are discussed here, and just noting somewhere (if important) that other variations did not show much change in the results. Also, if the text could explain the naming convention for the different simulations used, that would be much easier for the reader to interpret them.
In part because no results were shown from several simulations and in part because some parameter values were too extreme, we have adjusted the simulations. These changes are listed in a new Table 2:

Rime splintering				Ice-ice collisional breakup			
RS1:	$\aleph_{RS} = 300,$	$w_{RS} = \text{TR}$		**BR1ig**:	*graupel_breakup_ice*		
					$F_{BR} = 180,$	$T_{min} = 256,$	$\gamma = 3$
RS2:	$\aleph_{RS} = 300,$	$w_{RS} = \text{UNI}$		**BR2ig**:	*graupel_breakup_ice*		
					$F_{BR} = 360,$	$T_{min} = 249,$	$\gamma = 5$
				BR2sg:	*graupel_breakup_snow*		
					$F_{BR} = 360,$	$T_{min} = 249,$	$\gamma = 5$
Droplet shattering				**Combinations**			
DS1:	$\aleph_{DS} = 2,$	$p_{max} = 5\%,$	$\sigma = 3$	**RS2 + BR2ig**:	$\aleph_{RS} = 300,$	$w_{RS} = \text{UNI}$	
					graupel_breakup_ice		
					$F_{BR} = 360,$	$T_{min} = 249,$	$\gamma = 5$
DS2:	$\aleph_{DS} = 10,$	$p_{max} = 10\%,$	$\sigma = 5$	**DS2 + BR2ig**:	$\aleph_{DS} = 10,$	$p_{max} = 10\%,$	$\sigma = 5$
					graupel_breakup_ice		
					$F_{BR} = 360,$	$T_{min} = 249,$	$\gamma = 5$
				RS2 + DS2:	$\aleph_{RS} = 300,$	$w_{RS} = \text{UNI}$	
Control					$\aleph_{DS} = 10,$	$p_{max} = 10\%,$	$\sigma = 5$
CTRL:	$\aleph_* = 0$	$F_{BR} = 0$		**ALL**:	$\aleph_{RS} = 300,$	$w_{RS} = \text{UNI}$	
					$F_{BR} = 360,$	$T_{min} = 249,$	$\gamma = 5$
					*graupel_breakup_**		
					$\aleph_{DS} = 10,$	$p_{max} = 10\%,$	$\sigma = 7$

The previous naming schemes were based on the idea of four levels of experiments – **C**onservative, **M**oderate, **N**arrow, and **G**enerous – but this was not clear since there was no description in the manuscript. The idea had been to have a fractional factorial experimental design that probed the whole parameter space without an expensive, one-at-a-time approach. In the new scheme shown above, we have only defined two "levels" for each process to avoid the most extreme values we had used earlier, particularly for rime splintering and droplet shattering.

We have also condensed Figure 2 for the new simulation layout:

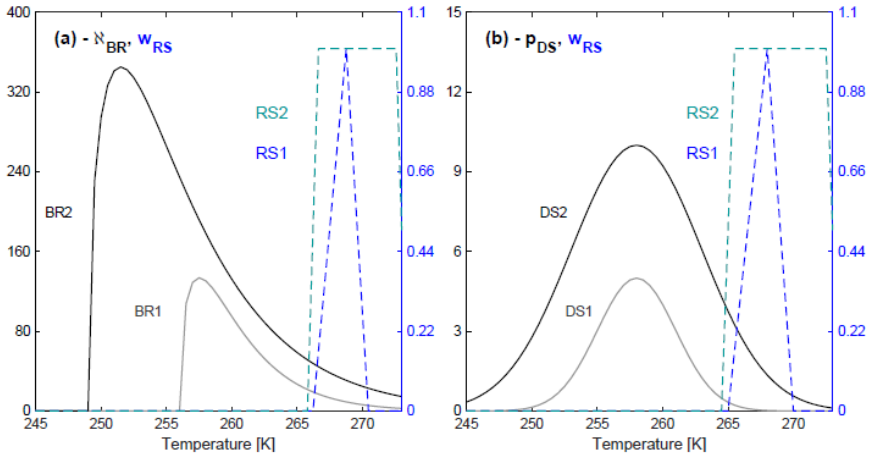

Figure 2 Fragment numbers, weightings, and probabilities from the secondary ice production parameterizations. In panel a, we show N_{BR} from both ice-ice collisional breakup simulations (BR1 and BR2) as well as the triangular and uniform $w_{RS}(T)$. In panel b, we show p_{DS} from both droplet shattering simulations (DS1 and DS2) and w_{RS} once again. The overlapping temperature regions of these are particularly important to understand any feedback between the processes.

If the major issues in this review are addressed, I suspect that much of the wording will be revised, and thus I will refrain from noting any suggestions at this time.

The effect of secondary ice production parameterization on the simulation of a cold frontal rainband

Sylvia C. Sullivan[1,2], Christian Barthlott[1], Jonathan Crosier[3], Ilya Zhukov[4], Athanasios Nenes[2,5,6], and Corinna Hoose[1]

[1]Institute of Meteorology and Climate Research, Karlsruhe Institute of Technology, Karlsruhe, Germany
[2]Department of Chemical and Biomolecular Engineering, Georgia Institute of Technology, Atlanta, GA 30332, USA
[3]School of Earth, Atmospheric, and Environmental Studies, University of Manchester, Manchester, UK
[4]Jülich Supercomputing Center, Forschungszentrum Jülich, Jülich, Germany
[5]ICE-HT, Foundation for Research and Technology, Hellas, 26504 Patras, Greece
[6]Institute of Environmental Research and Sustainable Development, National Observatory of Athens, 15236, Palea Penteli, Greece

Correspondence to: S. Sullivan (scs2229@columbia.edu), A. Nenes (athanasios.nenes@gatech.edu), C. Hoose (corinna.hoose@kit.edu)

Abstract. Secondary ice production via processes like rime splintering, frozen droplet shattering, and breakup upon ice hydrometeor collision have been proposed to explain discrepancies between in-cloud ice crystal and ice-nucleating particle numbers. To understand the impact of this ~~kind of additional ice number~~ additional ice crystal generation on surface precipitation, we present one of the first studies to implement frozen droplet shattering and ice-ice collisional breakup parameterizations in a ~~larger-scale~~ mesoscale model. We simulate a cold frontal rainband from the Aerosol Properties, PRocesses, And InfluenceS on the Earth's Climate campaign and investigate the impact of the new parameterizations on the simulated ice crystal number concentrations (ICNC) and precipitation. Near the convective regions of the rainband, contributions to ICNC can be as large from secondary production as from primary nucleation, but ICNCs greater than 50 L^{-1} remain underestimated by the model. Addition of the secondary production parameterizations also clearly intensifies the differences in both accumulated precipitation and precipitation rate between the convective towers and non-convective gap regions. We suggest, then, that secondary ice production parameterizations be included in large-scale models on the basis of large hydrometeor concentration and convective activity criteria.

1 Introduction

Cloud microphysics mediate precipitation formation, either from the in-cloud liquid or ice phase. In both cases, precipitation is observed to form much faster than the time frame to form sedimentable hydrometeors by solely condensational or depositional growth. Instead, accretional growth is required, be it collision-coalescence of liquid droplets, droplet riming on ice hydrometeors, or ice crystal aggregation. The efficiency of these processes is controlled by hydrometeor size through their terminal velocity and cross section within a collisional kernel (e.g., Rosenfeld and Gutman, 2001; Khain et al., 2005).

In clouds with high cloud condensation nuclei (CCN) concentrations, precipitation is more likely to initiate in the ice phase because cloud droplets will be smaller and less likely to grow to sedimentable size. This ice-initiated precipitation occurs often over the continents, where aerosol loadings are higher (e.g., Mülmenstädt et al., 2015; Lohmann, 2017), and in convective clouds for which the vertical motions are strong enough to carry droplets above the freezing level. Cold phase initiation has been associated with the top 10% of heavier rains according to data from the Tropical Rainfall Measuring Mission (Lau and Wu, 2011), and precipitation indices have been developed based upon cold cloud coverage (e.g. Arkin and Meisner, 1987; Joyce and Arkin, 1997). In these cases of ice-initiated precipitation, the requisite crystal growth can occur via riming or the Bergeron process, in which water vapor transfers from droplets to ice crystals under appropriate thermodynamic conditions. Ice hydrometeors eventually fall out of the cloud and reach an altitude at which they melt to form rain drops.

To accurately forecast cold phase-initiated precipitation, we must first accurately model in-cloud ice formation. Much effort has been devoted to understanding which atmospheric aerosols can act as ice-nucleating particles (INP) (e.g., Möhler et al., 2006; Knopf and Koop, 2006; Möhler et al., 2008; DeMott et al., 2010; Broadley et al., 2012; Hoose and Möhler, 2012; O'Sullivan et al., 2015; DeMott et al., 2016). But numerous measurements also indicate much larger in-cloud ice crystal number concentrations (ICNC) than INP numbers (e.g., Crawford et al., 2012; Heymsfield and Willis, 2014; Lasher-Trapp et al., 2016; Taylor et al., 2016). These kinds of ICNC 'enhancements' may be due to shattering upon impact with the probe inlet (e.g., Heymsfield, 2007; McFarquhar et al., 2007), but more recent measurements employ probe tips that reduce airflow disturbance around the inlet (Korolev et al., 2013a, b) and interarrival time (IAT) algorithms to filter out artifacts (Field et al., 2003, 2006; Korolev and Field, 2015). The ICNC-INP discrepancy remains in some cases, and a variety of secondary ice production processes have been proposed to make up the difference.

Given the linkage of cloud ice and precipitation, including these secondary ice production processes in meteorological models may yield more accurate precipitation forecasts. But the precipitation change with ICNC change will not always be the same, as schematized in Figure 1. For example, an additional source of small ice crystals would extend cloud duration and delay precipitation in a kind of cloud lifetime effect. But the depositional growth of these small ice crystals may also deplete supersaturation to a level at which the Bergeron process initiates. Then ice hydrometeors quickly become large, shortening cloud duration and accelerating precipitation. This pathway should be more important for stratiform precipitation, given the narrow range of requisite ambient vapor pressures: indeed for an integral ice radius of 100 μm cm^{-3}, the updraft must be less than about a 1 m s^{-1} for the Bergeron process to occur (Korolev, 2007). A 'cascade effect' has been proposed in which small ice crystals collide with large droplets, freezing and shattering them and forming more crystals (Lawson et al., 2015). ~~Or dynamic-microphysical~~ Dynamic-microphysical feedbacks could exist: an additional source of small crystals would generate more latent heat, changing the vertical heating profile and potentially affecting precipitation through altered detrainment rates or cloud updrafts (e.g. Clark et al., 2005). ~~Along with the~~ Efficient riming at mixed-phase temperatures may also simply generate larger hydrometeors that sediment more quickly, particularly in convective regions with a high degree of mixing. Along with these hydrological implications of altered precipitation, more glaciated clouds will be optically thinner and radiatively warm the surface.

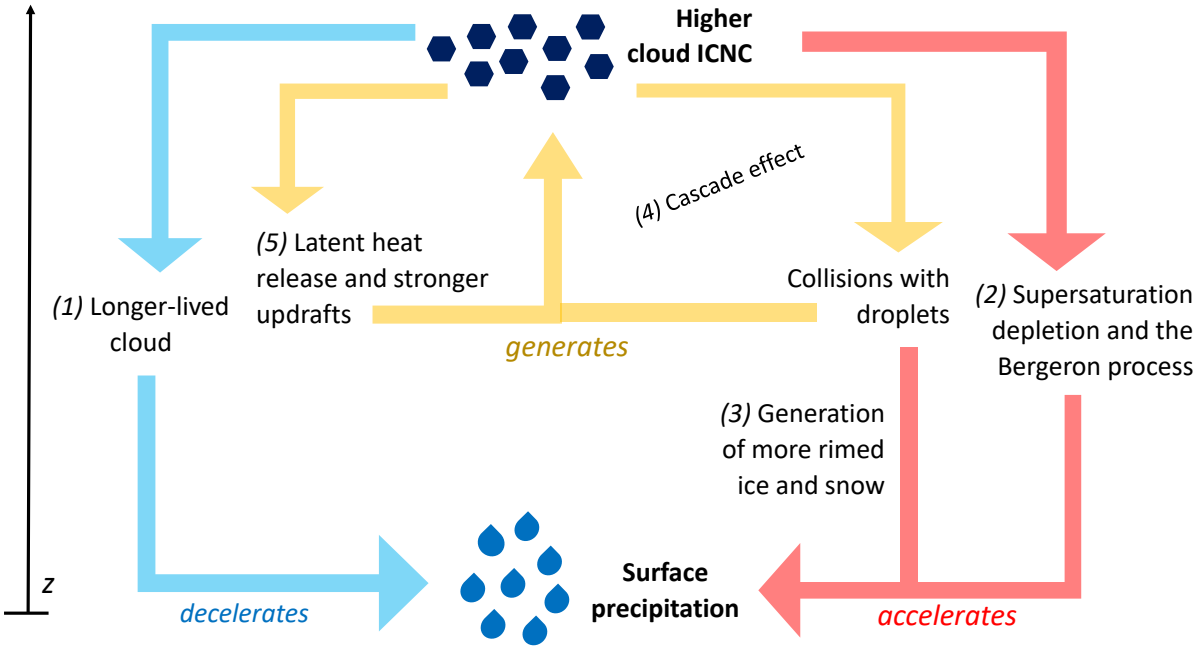

Figure 1. ~~Secondary production will generate higher ICNCs within~~ Within mixed-phase clouds, ~~but different feedbacks~~ ice and ~~impacts on~~ its secondary production will impact surface precipitation ~~are possible~~in various ways. Precipitation rates could decelerate via a cloud lifetime effect (1), where small crystals stay aloft longer, or accelerate via supersaturation depletion (2), where larger crystals grow at the expense of liquid droplets via the Bergeron process. More frequent riming may simply generate more large and dense hydrometeors that can fall out and melt to generate more surface precipitation (3). Additional crystals due to droplet freezing could also ~~collide, freeze, and shatter droplets in~~ generate a cascade effect (3~~4~~) ~~or strengthen~~ whereby the ~~updraft and supersaturation via their release~~ generation of more ice leads to more collisions with droplets that leads to generation of more ice. The latent heat ~~of fusion~~ release upon droplet freezing can also invigorate updrafts (4~~5~~).

Several studies have considered these linkages, both with measurements and models, but no consensus has been reached on their individual or net impacts. For example, ? Connolly et al. (2006b) did not see a large change in surface precipitation from a tropical thunderstorm when they altered the rime splintering rate in the Weather Research and Forecasting model. Dearden et al. (2016) also found that, in simulations of summertime cyclones, depositional growth of ice crystals was much more influential than inclusion of rime splintering on the spatial distribution of precipitation. On the other hand, an early study by Aleksić (1989) found that, in Serbia, more numerous ice crystals due to a hail suppression program led to more intense rainfall. Clark et al. (2005) discussed how the latent heating from additional ice generation modifies the vertical temperature profile, and hence precipitation rates. And Taylor et al. (2016) concluded that the combination of droplet coalescence and secondary ice production often determined precipitation timing and intensity in the maritime cumuli they observed. The kind of compensating effects discussed above, along with the insusceptibility of accretional processes to aerosol perturbations, would also reduce sensitivity of precipitation to aerosol more generally, as discussed in the study of Glassmeier and Lohmann (2016).

In this studyHere, we implement parameterizations of frozen droplet shattering and ice-ice collisional breakup, two proposed secondary production processes, into the Consortium for Small-Scale modeling (COSMO) framework described in Section 3. Frozen droplet shattering refers to a pressure build-up as a larger droplet freezes, either due to formation of an external ice shell or to latent heat of fusion release. This increased pressure eventually leads to spicule ejection or cracking and explosion of the ice shell (Leisner et al., 2014; Wildeman et al., 2017). In ice-ice collisional breakup, the impact of two ice hydrometeors leads to shattering, particularly of dendrites or fragile protuberances (Vardiman, 1978; Takahashi et al., 1995; Yano and Phillips, 2011). COSMO already includes a description of a third process called rime splintering (Hallett and Mossop, 1974). We investigate the impact of these parameterizations on the simulated ICNC and surface precipitation in a case study.

2 Parameterizations

2.1 Frozen droplet shattering parameterization

Recent droplet levitation experiments of Leisner et al. (2014) and high speed video from Wildeman et al. (2017) are elucidating the exact physics behind the shattering of droplets as they freeze . (Leisner et al., 2014; Wildeman et al., 2017). Droplet shattering has been previously parameterized statistically in a bin microphysics scheme with the fragment number as a function of drop diameter to the fourth power, using data from the Ice in Clouds Experiment - Tropical (ICE-T) campaign (Lawson et al., 2015, 2017). But while measurements continue to confirm a strong dependence of fragment number on droplet size, even recent studies could not confirm this fourth-power dependence (e.g. Lauber et al., 2018). The laboratory studies of Lauber et al. (2018) in particular add important quantitative results to existing secondary ice measurements but are taken at two droplet sizes (83 and 310 μm) so that it remains difficult to rigorously formulate fragment number. For now, we parameterize this process with the product of a fixed fragment number, a temperature-dependent shattering probability, and the existing droplet freezing tendency:

$$\left.\frac{\partial N_{ice}}{\partial t}\right|_{DS} = \left[1 + p_{DS}\aleph_{DS}\right]\frac{\partial N_{freez}}{\partial t} \tag{1}$$

$$p_{DS} = \frac{p_{max}}{\max\{\mathcal{N}(T_\mu,\sigma)\}}\mathcal{N}(T_\mu,\sigma) \tag{2}$$

$$\mathcal{N}(T_\mu,\sigma) = \frac{1}{\sqrt{2\pi}\sigma}\exp\left[\frac{-(T-T_\mu)^2}{2\sigma^2}\right] \tag{3}$$

~~We use a~~ A constant value for the ejected fragment number $\aleph_{DS}$ ~~because measurements of this value are ongoing. Future studies should add dependency on droplet size and perhaps temperature to this parameter. Shattering~~ is used, and shattering probability is given by a normal distribution in temperature, centered at a temperature T_μ of 258 K, with a default standard deviation σ of 3 K and default maximum probability p_{max} is 20%, similar to Sullivan et al. (2018). Examples of this distribution are shown in Figure 2b and d. Then $\partial N_{freez}/\partial t$ is the number of frozen raindrops for a given time step, predicted by the Bigg (1953) heterogeneous freezing parameterization (see Appendix A for details).

2.2 Ice-ice collisional breakup parameterization

~~Breakup upon ice hydrometeor collision is parameterized as the product of a fragment number generated upon collision and the existing~~ Vardiman first parameterized ice-ice collisional breakup using fragment generation functions based on the momentum exchange between two particles upon impact and leading coefficients dependent upon crystal type (Vardiman, 1978). More recently, Yano and Phillips (2011) and Yano et al. (2016) constructed a dynamical system-type models that tracks only ice crystal, small graupel, and large graupel number densities and illustrated the ability of ice-ice collisions to generate huge ice crystal enhancements in the absence of vapor limitation. Recently a more complete parameterization has used an exponential formulation with the initial kinetic energy of two particles, their temperature- and humidity-dependent collision type, and asperity fragility coefficients (Phillips et al., 2017b, a). We choose to focus on temperature dependence in a more straightforward, if less physically rigorous, product of fragment number and hydrometeor collision tendency:

$$\left.\frac{\partial N_{ice}}{\partial t}\right|_{BR,jk} = -\aleph_{BR}\left.\frac{\partial N_j}{\partial t}\right|_{coll,jk} \tag{4}$$

$$\aleph_{BR} = F_{BR}(T - T_{min})^{1.2}\ \exp\left[-(T - T_{min})/\gamma_{BR}\right] \tag{5}$$

$$\left.\frac{\partial N_j}{\partial t}\right|_{coll,jk} = -\frac{\pi}{4}\overline{E_{jk}}N_jN_k\left[\delta_j^0 D_j^2(\overline{x_j}) + \delta_{jk}^0 D_j(\overline{x_j})D_k(\overline{x_k}) + \delta_k^0 D_k^2(\overline{x_k})\right]$$
$$\times\left[\theta_j^0 v_j^2(\overline{x_j}) - \theta_{jk}^0 v_j(\overline{x_j})v_k(\overline{x_k}) + \theta_k^0 v_k^2(\overline{x_k})\right]^{1/2} \tag{6}$$

where the number of fragments generated $\aleph_{BR}$ is based upon the laboratory data of Takahashi et al. (1995) as in Sullivan et al. (2017). Within Equation 5, T_{min} is a minimum temperature below which no breakup occurs and γ_{BR} is the decay rate of fragment number at warmer subzero temperatures. The effect of these parameters, along with the leading coefficient F_{BR}, is illustrated in Figure 2a and c. The collisional tendency $\partial N_j/\partial t_{coll,jk}$ involves a collection efficiency E_{jk}; the number, mass,

Table 1. New subroutines in the two-moment scheme, containing the ice hydrometeor collision parameterizations, given as *collider_ breakup_ collided*.

	ice crystals	**snow**	**graupel**	**hail**
ice crystals			*graupel_ breakup_ ice*	*hail_ breakup_ ice*
snow			*graupel_ breakup_ snow*	
graupel	*graupel_ breakup_ ice*	*graupel_ breakup_ snow*		*hail_ breakup_ graupel*
hail	*hail_ breakup_ ice*		*hail_ breakup_ graupel*	

and terminal velocities of the colliding hydrometeors; and nondimensional values δ^0 and θ^0 from a gamma size distribution (see Appendix B for details). The parameterization works with four ice hydrometeor classes, shown in Table 1, by designating one hydrometeor class as the 'collider' (j) and a second as the 'collided' (k). The number in the 'collided' class is increased by $\aleph_{BR}$, while that in the 'collider' class remains constant. Mass in both classes remains unchanged. Future studies could include collisions between all hydrometeor classes or redistribute number and mass between the 'collider' and 'collided' differently. These considerations could also be obviated by implementing the parameterization within a property-based ice microphysics scheme like the Predicted Particle Properties (P3) scheme (Morrison and Milbrandt, 2015; Milbrandt and Morrison, 2015). P3 tracks ice mixing ratio, number, mass, and rime fraction rather than number and mass in snow, graupel, and ice crystal categories whose thresholds can be non-physical. We expect a strong influence of temperature from our breakup tendency $(\partial N_{ice}/\partial t)_{BR,jk}$ than was discussed in Phillips et al. (2017a), given the direct and sole dependence in Equation 6.

2.3 Rime splintering parameterization

The existing parameterization of rime splintering is a product of a leading coefficient, a temperature-dependent weighting, and a rime mixing ratio:

$$\left.\frac{\partial N_{ice}}{\partial t}\right|_{RS} = \aleph_{RS} w_{RS} q_{rim}. \tag{7}$$

A default value of 3.5 $\times 10^8$ fragments per kilogram of rime, $\aleph_{RS}$, is used base on the experiments of Hallett and Mossop (1974). q_{rim} denotes the rime mixing ratio, and w_{RS} denotes a temperature-dependent weighting for rime splintering, which is triangular (TR) between 265 and 270 K by default and shown in Figure 2a and b. ~~Several other options for this temperature weighting have been added and are shown in Figure 2c: a shifted triangular weighting between 255 and 260 (**SH**) ; two broadened ones between 255 and 270~~ We add a second, uniform temperature weighting (~~**BR1** and **BR2**); a symmetric one centered at 262 (**SH**); and a uniform one between 255 and~~ UNI) between 263 and 273 K to investigate the possibility of a droplet shattering or ice-ice collisional breakup 'trigger' that feeds into a rime splintering 'cascade'. The rimer surface temperature may in fact be the more important factor and can remain between 265 and 270 K~~(**UNI**). Although observations indicate that rime splintering occurs at warm subzero temperature, primarily above 265 , we are interested in capturing any kind of cascadeeffect, as mentioned above. One can imagine a scenario in which even minimal rime splintering generates enough~~

ice to collide with droplets, freezing and then shattering them. These splinters could then go on to collide with, freeze, and shatter other droplets in a runaway cloud glaciation.

Finally, we , even for cloud temperatures a few degrees colder (Heymsfield and Mossop, 1984). We also limit rime splintering to occur only after collisions between cloud droplets of diameter greater than 25 μm or raindrops and ice crystals, graupel, or hail, assuming that the smaller size of cloud droplets and the slower terminal velocity of snow do not lead to the fragile frozen protuberances that easily splinter (e.g., Choularton et al., 1980; Mossop, 1985)hail, or snow (e.g., Phillips et al.; Connolly et al., 2006a) .

3 Simulations

These parameterizations and adjustments are implemented into the Consortium for Small-Scale modeling (COSMO) framework version 5.03 (Baldauf et al., 2011; Doms and Baldauf, 2015) that employs the two-moment microphysics scheme of Seifert and Beheng (2006) (SB06 hereafter). Several sensitivity tests are run, as listed in Table 2 and visualized in Figure 2. Simulation names include an 'A' if they employ the droplet shatteringparameterization and a 'B' if they employ the **RS** for rime splintering, **DS** for droplet shattering, or **BR** for ice-ice collisional breakupone. Two sets of parameters, one weaker (denoted **1**) and one stronger (denoted **2**), are defined for each tendency. We also run a set of combination simulations in which multiple or all of the secondary ice parameterizations are simultaneously activated (**RS+BR**, **RS+DS**, **DS+BR**, and **ALL**) and a control simulation in which all secondary ice production processes, including the default rime splintering in SB06, are turned off (denoted **CTRL** throughout). Set 1 adjusts the fragment number formed per milligram of rime $\aleph_{RS}$ within the rime splintering parameterization; Set 2 adjusts the ice hydrometeor classes that collide; and Set 3 adjusts the parameters within the collisional breakup parameterization. For each simulation, an ensemble of 10 5 runs is done with "stochastically perturbed physics tendencies" (e.g., Buizza et al., 1999), applied to vapor, cloud, and ice mixing ratio tendencies, and the ensemble mean output and standard deviation are evaluated. A control simulation with the standard Seifert and Beheng microphysics scheme is also run and denoted 'CTRL' throughout.

We use these parameterization configurations to simulate 3 March 2009 for a domain centered at 53°N, 5°W, with longitudes ranging from 65°N down to 46°N and latitudes ranging from 18°W to 10°E. In-situ cloud ice data and remote-sensing rainfall data are available for this case from the Aerosol Properties, PRocesses And InfluenceS on the Earth's climate (APPRAISE) campaign and Chibolton Chilbolton Facility for Atmospheric and Radio Research (CFARR) in Southern England respectively. The observations showed the passage of a narrow cloud frontal rain band over the UK around 1800 18:00 UTC and CFARR at 2000 20:00 UTC. These data have been thoroughly analyzed by Crosier et al. (2014).

The COSMO interpolation utility (INT2LM) was used to construct initial and boundary conditions from the 7-km COSMO-EU operational assimilation cycle analyses. All simulations are done at 2.8 km spatial resolution with a time step of 25 seconds, 50 vertical levels, and half-hourly output resolution. The Aerosol and Reactive Trace gases module (ART) is turned off. The Phillips et al. (2008) parameterization (PDA08) is used for primary ice nucleation, and the intermediate CCN level of the Segal and Khain parameterization is applied (Segal and Khain, 2006). Previous studies have noted that limited nucleating efficiencies

Table 2. Sensitivity tests are listed with $\aleph_{RS}$ in units of (mg rime)$^{-1}$ and T_{min}, σ in ~~units of K; results from runs enclosed in parentheses are not visualized~~Kelvin.

Rime splintering					**Ice-ice collisional breakup**	
~~**Set 1A**~~**1Ag****RS1**:	$\aleph_{RS}$ = ~~3000~~300,	w_{RS} = TR	~~**Set 2B**~~	~~**2Big**~~**BR1ig**:	*graupel_breakup_ice*	
					F_{BR} = 180,	T_{min} = 256,
~~**1Ac**~~**RS2**:	$\aleph_{RS}$ = 300,	w_{RS} = UNI		~~**2Bgh**~~**BR2ig**:	*graupel_breakup_ice*	
	~~**1Am**:~~	~~$\aleph_{RS}$~~			F_{BR} = ~~850~~360,	T_{min} = 249,
				~~**2Bih**~~**BR2sg**:	*graupel_breakup_snow*	
	~~**1An**:~~	~~$\aleph_{RS}$~~			F_{BR} = ~~3000~~360,	T_{min} = 249,
	~~**2Bsg**:~~	**Droplet shattering**			**Combinations**	
~~**Set 3A**~~**3Ag****DS1**:	$\aleph_{DS}$ = 2,	p_{max} = ~~40~~5%,	~~$\aleph_{DS}$~~ σ = ~~100~~3	**RS2 + BR2ig**:	$\aleph_{RS}$ = 300,	~~σ~~ w_{RS} = ~~12~~UNI
	~~**3Bg**:~~				*graupel_breakup_ice*	
					F_{BR} = 360,	T_{min} = 249,
~~**3Ac**~~**DS2**:	$\aleph_{DS}$ = 10,	p_{max} = ~~5~~10%,	σ = 5	**DS2 + BR2ig**:	$\aleph_{DS}$ = ~~2~~10,	p_{max} = 10%,
		~~**3Bc**:~~			*graupel_breakup_ice*	
					F_{BR} = ~~40~~360,	T_{min} = ~~257~~249,
				~~**3Am**~~**RS2 + DS2**:	~~p_{max}~~ $\aleph_{RS}$ = ~~10%~~300,	w_{RS} = UNI
	Control				$\aleph_{DS}$ = 10,	p_{max} = 10%,
CTRL:	$\aleph_{*}$ = 0	~~F_{BR} = 0~~		~~**3Bm**~~**ALL**:	~~F_{BR}~~ ~~$\aleph_{RS}$~~ = ~~180~~300,	~~T_{min}~~ w_{RS} = ~~256~~UNI
	~~**3An**:~~	~~p_{max}~~			F_{BR} = ~~25%~~360,	~~$\aleph_{DS}$~~ T_{min} = ~~100~~249,
		~~**3Bn**:~~	~~F_{BR}~~		*graupel_breakup_**	
					$\aleph_{DS}$ = ~~500~~10,	~~T_{min}~~ p_{max} = ~~258~~10%,

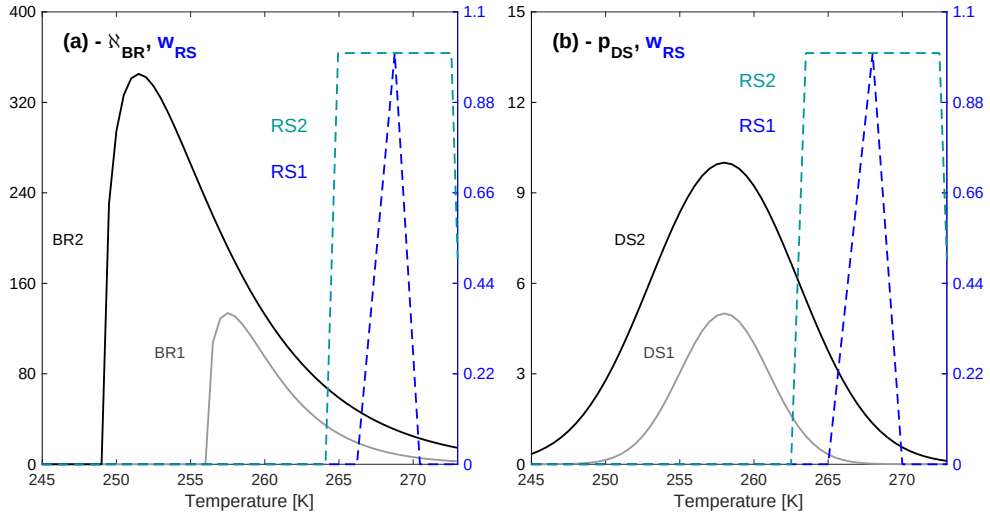

Figure 2. Fragment numbers, weightings, and probabilities from the secondary ice production parameterizations. ~~The default fragment number~~ In panel a, we show $\aleph_{BR}$ from both ice-ice collisional breakup ~~$\aleph_{BR}$~~ simulations ~~(used in Set 2B)~~ BR1 and ~~rime splintering weighting w_{RS} are shown in panel (a~~BR2) ~~versus temperature~~as well as the triangular and uniform $w_{RS}(T)$. ~~Panel~~ In panel b~~shows w_{RS} again~~, ~~overlapping the probability of a frozen~~ we show p_{DS} from both droplet shattering ~~p_{DS}~~ simulations ~~(used in Set 1A~~DS1 and DS2) ~~, in percent~~and w_{RS} once again. The ~~various $\aleph_{BR}$ functions used in the Set 3B simulations~~ overlapping temperature regions of these are ~~shown in panel (c);~~ particularly important to understand any feedback between the ~~various p_{DS} functions in Set 3A in panel (d); and the various w_{RS} functions in Set 1A in panel (e)~~processes.

in the PDA08 may lead to underestimation of ICNC at mixed-phase conditions (Barahona et al., 2010; Curry and Khvorostyanov, 2012; Mo
. No ice nucleating particle (INP) measurements were made during this case study, but from other observational datasets,
PDA08 still yields better agreement with in-situ ICNCs than purely lab-based or theoretical parameterizations (Sullivan et al., 2016)
. Crosier et al. (2014) also note that the low cloud top temperatures and strong updrafts in convective regions generate supersaturations
that could favor large ice production from homogeneous nucleation. While not observationally confirmed, these conditions
could buffer the ice nucleation tendency to our choice of parameterization.

The rainband structure allows us to investigate multiple secondary production processes at the same time because it contains regions with varying dynamic and thermodynamic conditions. For example, large liquid water contents and stronger updrafts are favorable for frozen droplet shattering (Lawson et al., 2015; Taylor et al., 2016), and these conditions can be found in the narrow leading edge. For rime splintering, lower updrafts and liquid water contents and bimodal droplet size distributions are favorable (e.g. Choularton et al., 1980; Mossop, 1985; Heymsfield and Willis, 2014), and these conditions are found at the top of convective turrets and in the trailing region of stratiform precipitation. The rainband vertically spans the optimal temperature zones for both droplet shattering and rime splintering (Hallett and Mossop, 1974; Leisner et al., 2014; Lawson et al., 2015) and horizontally spans both maritime and continental zones to compare any impact of different surface heat budget.

4 Results

4.1 ~~Impact on ice crystal production~~Dynamic environment

We begin by comparing the observed and modeled dynamics to understand how these differences may impact later microphysical ones. We show the updraft along a 255° radial out from the CFARR station (Figure 3) as in Figure 5d of Crosier et al. (2014) . Comparison to simulations cannot be exact, as the output from the model exists along a coarser spatiotemporal grid. We use those w values whose latitude-longitude pair minimizes the Euclidean distance to the precise values along the radial. Thereafter we interpolate both over distance and altitude on a 1000 x 500 grid to generate the range-height indicator (RHI)-type plot. This interpolation leads both to intermittent discontinuities and to weakening of extremes. The upright updraft region about 60 km from CFARR appears distinctly in the simulated field but with vertical velocity magnitude far smaller (and extent far greater) than those derived from measurements (maximum of about 1 m s^{-1} relative to about 6 m s^{-1}). Downdrafts of more similar magnitude and extent to those observed also form in adjacent regions. Values derived from Doppler velocities (v_u) also rely on an assumption that at low elevation, v_u approximates the horizontal wind and that any convergence or divergence of these horizontal winds within discrete columns must conserve mass with a compensating upward or downward velocity.

Comparison of the surface wind speed both in the CTRL simulation and from a three cup anemometer at CFARR is also shown in Figure 3b. Three series are shown from the simulation at latitude and longitudes closest to the center. Simulated wind speed peaks too early but to a value only slightly less than the average of the observations. Both series display a sudden drop in the strength of these winds with similar decay rates and plateau values of about 5 m s^{-1}. Perhaps most important is the consistent underestimation of these surface winds prior to the rainband event, from 17:00 to 19:00 UTC. Given that the direction of low-level winds preceding the rainfall event was southwesterly (Crosier et al. (2014), their Figure 4b), underestimating their magnitude will diminish the oceanic moisture advection and moisture source ultimately available to form rain over the continent.

Figures 3c and d also show the vertical velocities in the CTRL simulation at altitudes of 1 and 7 km at 18:00 UTC as the rainband reaches land. Its structure is apparent in the low-level updrafts of about 1 to 2 m s^{-1} (although these are again much weaker than those from observations) and their adjacent downdrafts with similar magnitudes of opposite signs. Elsewhere values are $\pm$ 0.2 m s^{-1} with slow descent presiding. For the upper-level field that corresponds to cloud top, the highest ascending motions also occur around the rainband region and slow ascent ($\leq$ 0.4 m s^{-1}) dominates.

We next compare range-height indicator (RHI) scans of radar reflectivity (Z_{DR}) from the Chilbolton Advanced Meteorological Radar (CAMRa) and the CTRL simulation (Fig.4). The CAMRa is a 3 GHz Doppler instrument with a 0.28° beam, and its scan between 19:22:07 and 19:23:07 UTC along the 255° radial out from CFARR is shown, as in Figure 5a of Crosier et al. (2014) . We use output from 19:00:00 UTC in the CTRL simulation and again identify the modeled latitude-longitude pair that minimizes the Euclidean distance to the exact value from along the 255° radial. We then perform bilinear interpolation on the simulated values of Z_{DR} over a 1000 distance x 500 altitude grid.

The CAMRa scan shows the location of cloud top height and convective activity: the lowest Z_{DH} is around 6 to 8 km and fall streaks are present moving toward the CAMRa. These Z_{DH} fall streaks, as well as those in differential reflectivity (shown

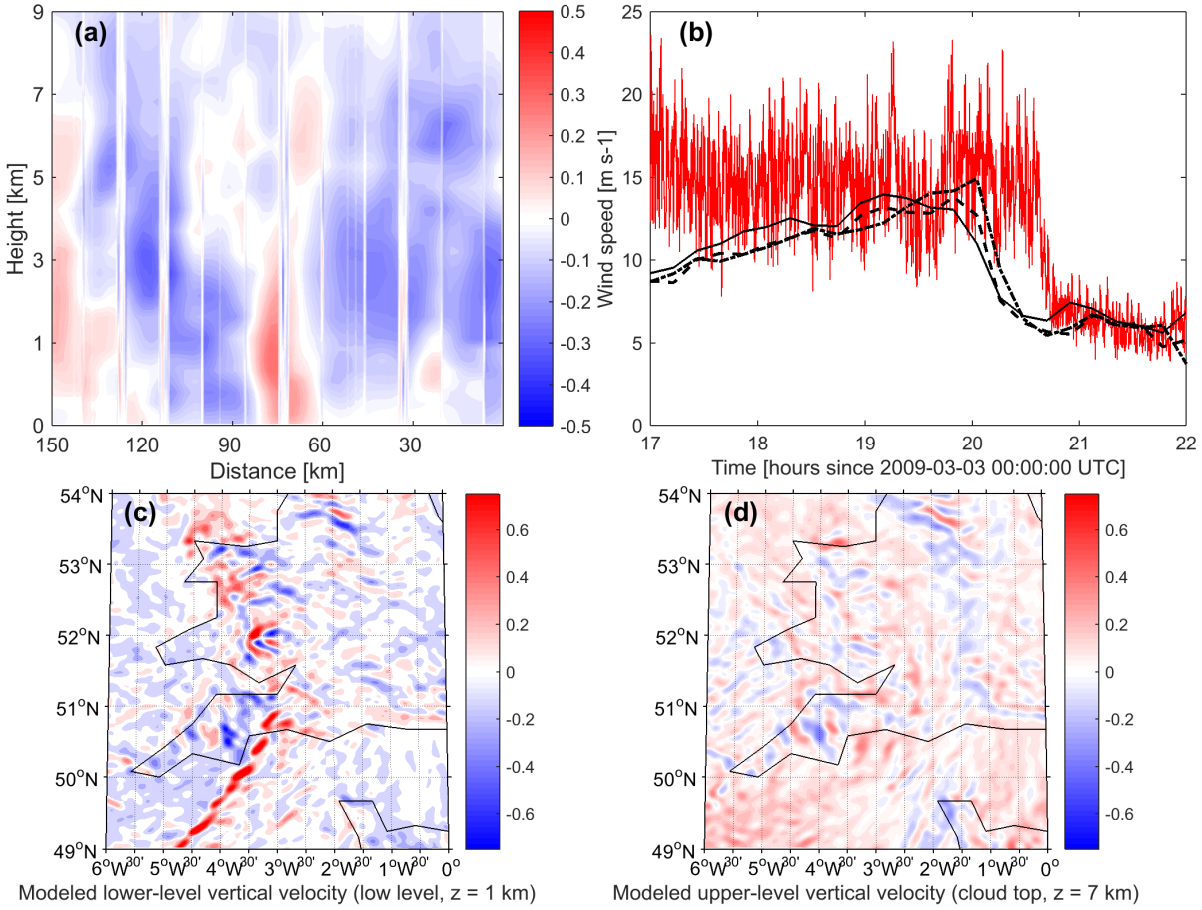

Figure 3. Different model dynamical fields. In panel a, we show the updraft velocity 150 km along the 255° radial from CFARR at 51.1°N, 1.4°W with values from the CTRL simulation at 19:00 UTC. Discontinuities are due to the minimization of Euclidean distance or interpolation aspects of an algorithm to approximate the radial from the model discretization. Surface wind speeds from 17:00 to 22:00 UTC from the CFARR three cup anemometer and our CTRL simulation are shown in panel b. Panels c and d show the modeled vertical velocities from the CTRL simulation at 1 and 7 km respectively at 18:00 UTC as the rainband began to pass over the UK.

in Crosier et al. (2014), their Fig. 5c) are signatures of ice crystal sedimentation and aggregation near cloud top. Ice crystal seeding may also be occurring with lower-level sedimentation, but the altitudinal peak in $N_{i,prj}$ does not fall consistently above that in N_{ice} (Figs. S3 and S4) and secondary ice production must also generate a portion of this low-level ice. Intermediate values of Z_{DH} occur at altitudes of 2 to 5 km, and the highest ones occur around the melting layer at 1 to 2 km, as discussed by Crosier et al. (2014). General features are replicated in the simulated reflectivities. Very low Z_{DH} occur close to CFARR with cloud top around 7 km, but further out – around 70 to 100 km along the radial – these same very low reflectivities occur more often than in the measurements. The gradient to higher Z_{DH} at lower altitudes is also apparent in simulations, but not as distinct fall streak structures. Z_{DH} has increased to about 10 dBZ$_h$ by a height of 4 km and about 20 dBZ$_h$ by a height of 2 km. The highest reflectivities also fall in the same altitudinal range, but importantly do not have the same maximum as in the observations. Z_{DH} in an updraft core 60 km from CFARR reaches a value of 45 dBZ$_h$ in the CAMRa but only 30 dBZ$_h$ in the CTRL simulation. This may be due to underestimation of graupel formation or too high CCN or INP concentrations that delay precipitation in the base COSMO model (e.g. Baldauf et al., 2011). In Figure S1, we also show radar comparisons for the simulations with secondary ice parameterizations in place (RS1, DS1, BR1ig). These exhibit Z_{DH} of lower magnitude than the observations, even more so in the first 50 km extending from the CFARR site. We keep these underestimation in mind in the proceeding discussion of microphysical adjustments.

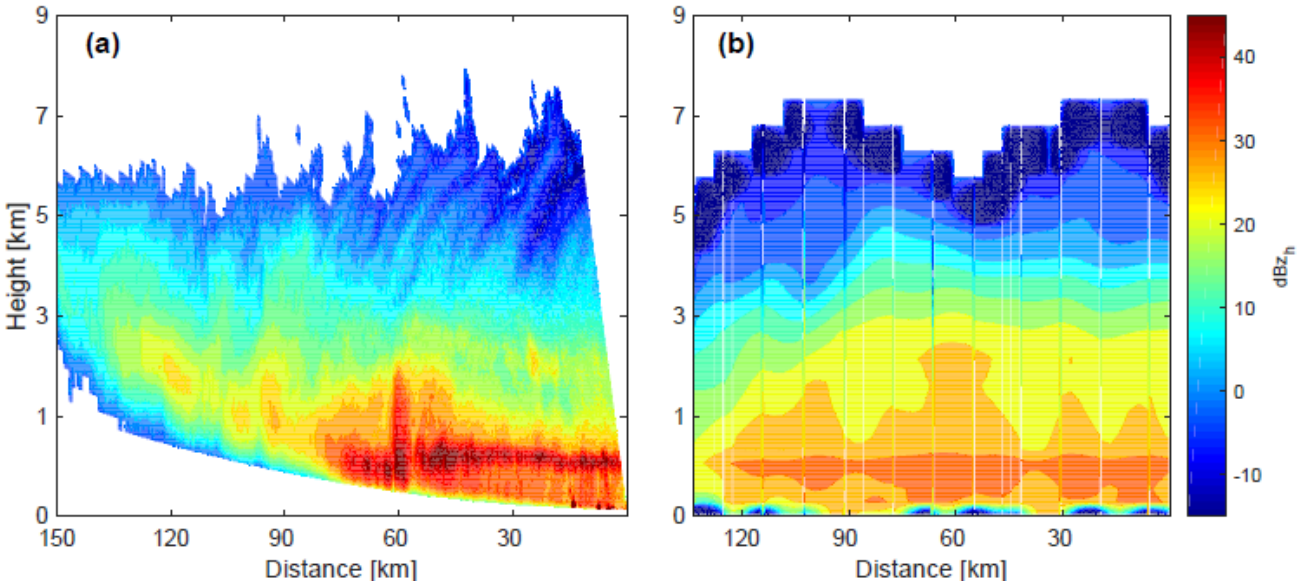

Figure 4. Model-measurement intercomparison of range-height indicator scans of radar reflectivity Z_{DH} along the 255° radial out from CFARR. CAMRa Doppler radar measurements are shown in panel a for the scan taken between 19:22:07 and 19:23:07 UTC, and modeled values are shown from the CTRL simulation at 19:00:00 UTC, both in dBZ$_h$.

4.2 Ice crystal production

We first present the spatial fields of secondarily-produced ICNC, $N_{i,sec}$, and ~~these values relative to the~~ the corresponding fields of primarily-nucleated ICNC, $N_{i,pri}$, at a single ~~pressure~~ level in Figure 5. ~~The pressure level is chosen to maximize this $N_{i,sec}$, and simulations 1Ag and 1Ac are shown with both frozen droplet shattering and rime splintering at different $\aleph_{RS}$ and w_{RS}. The 1Am and 1An simulationscontain intermediate values and are not shown~~An altitude of 3 km is chosen so that the temperature falls in the rime splintering temperature range ($T \in$ [249 K, 270 K] with a median value of 258 K), and we show first the rime splintering simulations. $N_{i,sec}$ is an accumulated ICNC from the secondary ~~production processes between 1800 and 1900~~ ice production between 18:00 and 18:30 UTC, as the cold frontal rainband begins to pass over the UK, and does not include any sedimentation loss to lower levels ~~to~~ or gain from higher ones. ~~The characteristic comma shape of clouds within a well-developed mid-latitude cyclone is apparent in panels a and b, and~~ In addition, we have filtered out all values less than 10^{-3} L^{-1} to give a clearer signal of where significant production occurs.

ICNC of up to ~~10^5~~ 1000 L^{-1} are produced over the half hour ~~. The structure~~ and over much of the domain. Banded structures appear in $N_{i,sec}$ ~~follows the rainband structure because it is contingent upon the large hydrometeors formed in the convective regions. Particularly for the rime splintering, mixing of young and old thermals at the top of convective towers may generate the bimodal droplet size distribution that seems to make the process more efficient (Mason and Jonas, 1974; Korolev, 1994)~~off the southern coast of the UK, where the largest raindrop number concentrations (Fig. S5d) and the highest updrafts at lower levels (Fig. 3c) occur. Underestimation of the updrafts within the rainband core (Sec. 4.1) will lead to errors that offset each other somewhat: too few raindrops will form when the vertical velocity and supersaturation are too low, but these will also be lofted more quickly through the altitudinal band where rime splintering is favorable, leaving less time for collisions.

In spatial maps of graupel and snow mixing ratios (Fig. S5), and to a lesser degree in panels a and b, the characteristic comma shape of clouds in a well-developed mid-latitude cyclone is apparent. Although graupel was absent throughout much of the observations, simulated graupel mixing ratio is non-negligible (greater than 0.25 g kg^{-1}) at low altitudes coincident with the rainband. The snow mixing ratio is also from 0.25 to 0.35 g kg^{-1} but at higher altitudes. It is likely then that much of the riming occurred on snow, as suggested by Crosier et al. (2014), and fell to lower altitudes with some portion splintering during descent.

In the ~~1Ac simulation, however, the~~ RS2 simulation, large values of $N_{i,sec}$ are found ~~not only in the rainband region, but also over Ireland and the adjacent North Atlantic. In fact, the spatial extent of large $N_{i,sec}$ is greater with the more conservative 1Ac simulation than the 1Ag one with larger $\aleph_{RS}$ and w_{RS}. A uniform temperature weighting in 1Ag allows the secondary ice generation to occur over more altitudes, so that the remaining rime mixing ratio in the air reaching this pressure level in the 1Ag simulationmay be somewhat lower than that in the 1Ac simulation. While the total horizontal extent of large $N_{i,sec}$ is greater in 1Ac than in 1Ag, the production region right around the rainband is more defined: in regions of high liquid water content, further north than in the RS1 simulation. For example, over~~ the ~~rime mixing ratio is unlikely to be depleted and~~ cold waters of the North Sea and Irish Sea, the rime splintering contribution moves to lower altitudes for the more limited temperature weighting w_{RS} in the ~~1Ag simulation does indeed produce higher $N_{i,sec}$.~~ RS1 simulation. The same is true for much of the

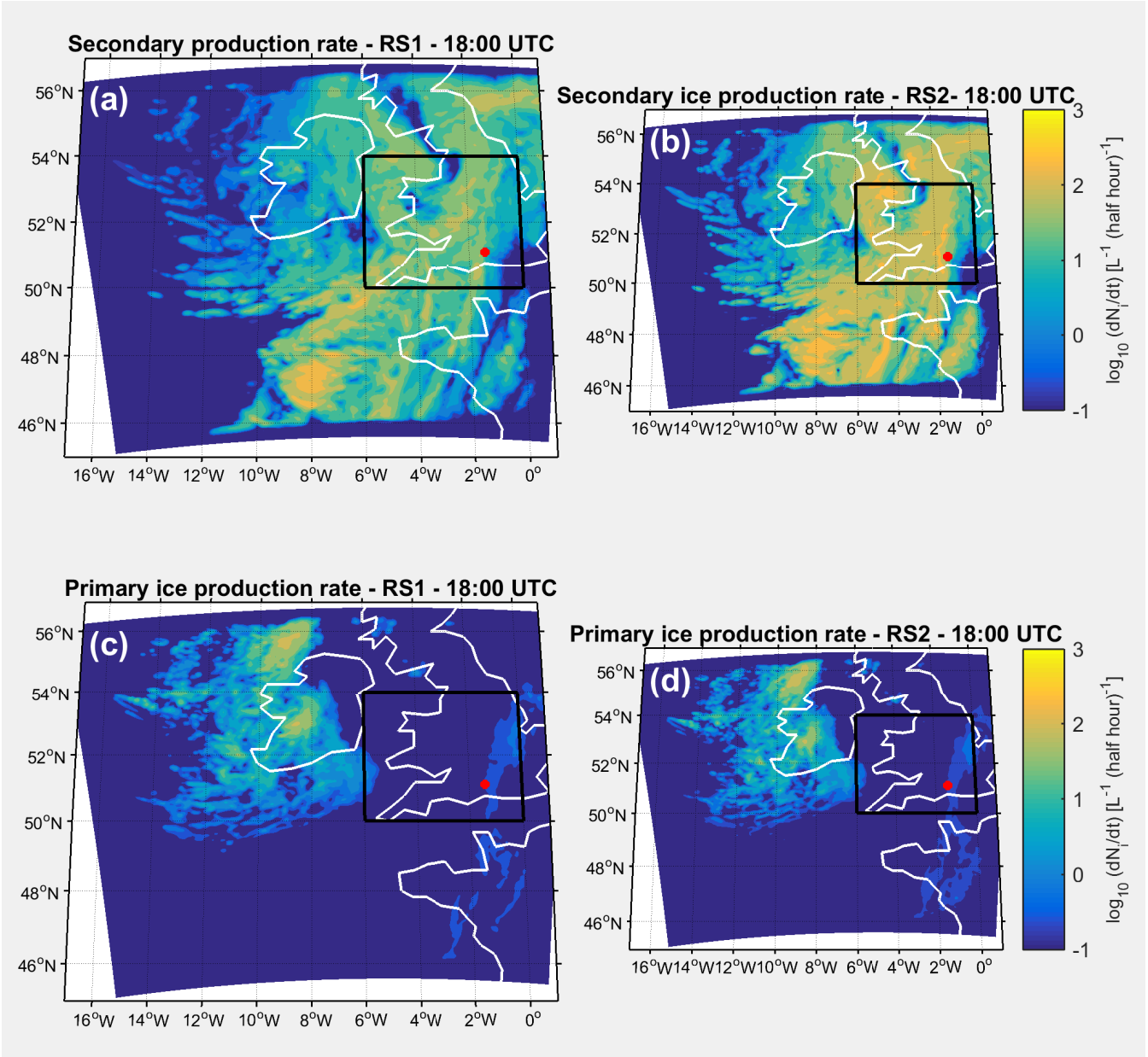

Figure 5. Maps of secondarily-produced ice from the ~~1Ag~~ RS1 (on the left) and ~~1Ac~~ RS2 (on the right) simulations at the ~~pressure levels~~ altitude where ~~$\overline{T} \approx$~~ rime splintering contributions are larger. Temperatures at this altitude fall between 249 K and 270 K with a median value of 258 K~~, as the rainband began to pass over the UK~~. Panels a and b show the number of secondarily-produced ice crystals from ~~1800~~ 18:00 UTC to ~~1900~~ 18:30 UTC, and panels c and d show the ~~ratio of secondarily-produced to~~ primarily-nucleated ICNCs for the same time period, as the rainband began to pass over the UK. Note the logarithmic colorbar. The black box shows the subdomain used in Figure ~~4~~7, and the red dot is the CFARR location.

continental ice production. In some instances of moisture limitation, we might expect that an extended w_{RS} actually decreases the rime splintering contributions at lower altitudes, as the rime mixing ratio may be depleted above. In this case, however, for a primarily oceanic domain, limited adjacent land, and strong surface winds (Fig. 3b), moisture advection is not limited.

~~Adjustments to the spatial distribution of ice formation will have energetic implications. If secondary ice production occurs over a great altitudinal depth,~~ For comparison, we show the corresponding primary ice nucleation fields in panels c and d. Again we filter out where these values are less than 10^{-3} L^{-1}. Much of the low-level ice comes from secondary production, although the temperatures at this altitude are still low enough for various aerosol to act as INP. In the rainband region, $N_{i,pri}$ is negligible and only in a small region in the northwest of the domain does it reach 100 to 1000 L^{-1}. The magnitude of these values is subject to uncertainty from the ~~small ice crystals are more likely to be advected into an outflow region where they will contribute to cirrus optical thickening and warming. Crosier et al. (2014) note the fallstreaks at cloud top of this rainband in their Doppler radar measurements. There are not heating effects directly associated with the rime splintering process. But higher ICNCs do make droplet riming more likely, so an indirect effect from heat of fusion release exists. Zhu et al. (2017) recently showed that melting over a greater depth strengthens the vertical advection of moisture, so it might be expected that freezing over greater depth would suppress this vertical moisture transport. But existing studies indicate that more intense detrainment may be the more important effect from freezing (Sud and Walker, 2003). Varying aerosol concentrations and surface radiative budgets over continental versus maritime environments could also affect ICNC. For example, secondary production should be less likely over continental regions with higher aerosol loadings because more and smaller cloud droplets form, diminishing the riming and droplet freezing efficiencies. In this case, however, no notable differences appear in the spatial snapshots of Figure 5~~nucleation parameterization, which, as noted above, has underestimated INP numbers in previous studies.

~~To gauge the importance of including these additional ice sources,~~ Next, we consider the relative ice crystal number concentrations produced by different processes in Figure 6. The largest $N_{i,sec}$ ~~accumulation can be compared to $N_{i,pri}$. In panels c and d, $N_{i,sec}/N_{i,pri}$ ranges from 0.1 to 10, particularly in the simulation with higher $\aleph_{RS}$ and w_{RS}. The higher values of~~ magnitudes, up to 1000 L^{-1} over the half hour, come from the RS1 and ALL simulations. These are followed by about 10 L^{-1} (half hour)$^{-1}$ generation rates from frozen droplet shattering and 0.1 L^{-1} (half hour)$^{-1}$ of snow and graupel. There is also an altitudinal hierarchy. Contributions from droplet shattering are largest at the highest altitudes of 4.5 km where raindrop number concentrations are still relatively high and the ~~ratio occur in the wide, trailing region of the rainband and in the 1Ag simulation, but still in a limited region. In simulations with ice-ice collisional breakup (not shown) , $N_{i,sec}$ is 100-fold smaller and the~~ temperature ($T \in$ [237 K, 262 K] with a median of 249 K) is cold enough for non-negligible shattering probability. The rime splintering contribution is next at an altitude of 3 km, and the breakup is largest at a lower altitude of 1.5 km because the graupel mixing ratio is highest here.

If graupel were present at higher altitudes, $N_{i,sec}$ ~~/$N_{i,pri}$ ratio is less than one in all regions. The liquid-dependent secondary production processes are more important in the case of the rainband, given the prevalence of large droplets and relative absence of either graupel or hail (Crosier et al., 2014). A means of including secondary ice production in larger-scale models, then, could be to include the parameterizations on the basis~~ from breakup could increase significantly, as both the snow mixing ratio and fragment number parameter increase at colder temperatures. Similarly very limited raindrop number concentrations exist at

the altitude where shattering probability is non-negligible. This importance of large hydrometeor number ~~criteria~~concentration for $N_{i,sec}$ suggests a means of parameterizing secondary ice production as meso- and large-scale models transition toward two-moment cloud schemes: the droplet shattering and collisional breakup parameterizations could be ~~turned on within the microphysics scheme~~ activated only for those cloudy grid cells with ~~greater than a certain~~ more than a threshold concentration of large droplets and graupel, hail, or snow respectively. In one-moment schemes, parameterizations on the basis of favorable thermodynamic regimes will be more useful for the time being.

~~Along with the spatial field~~

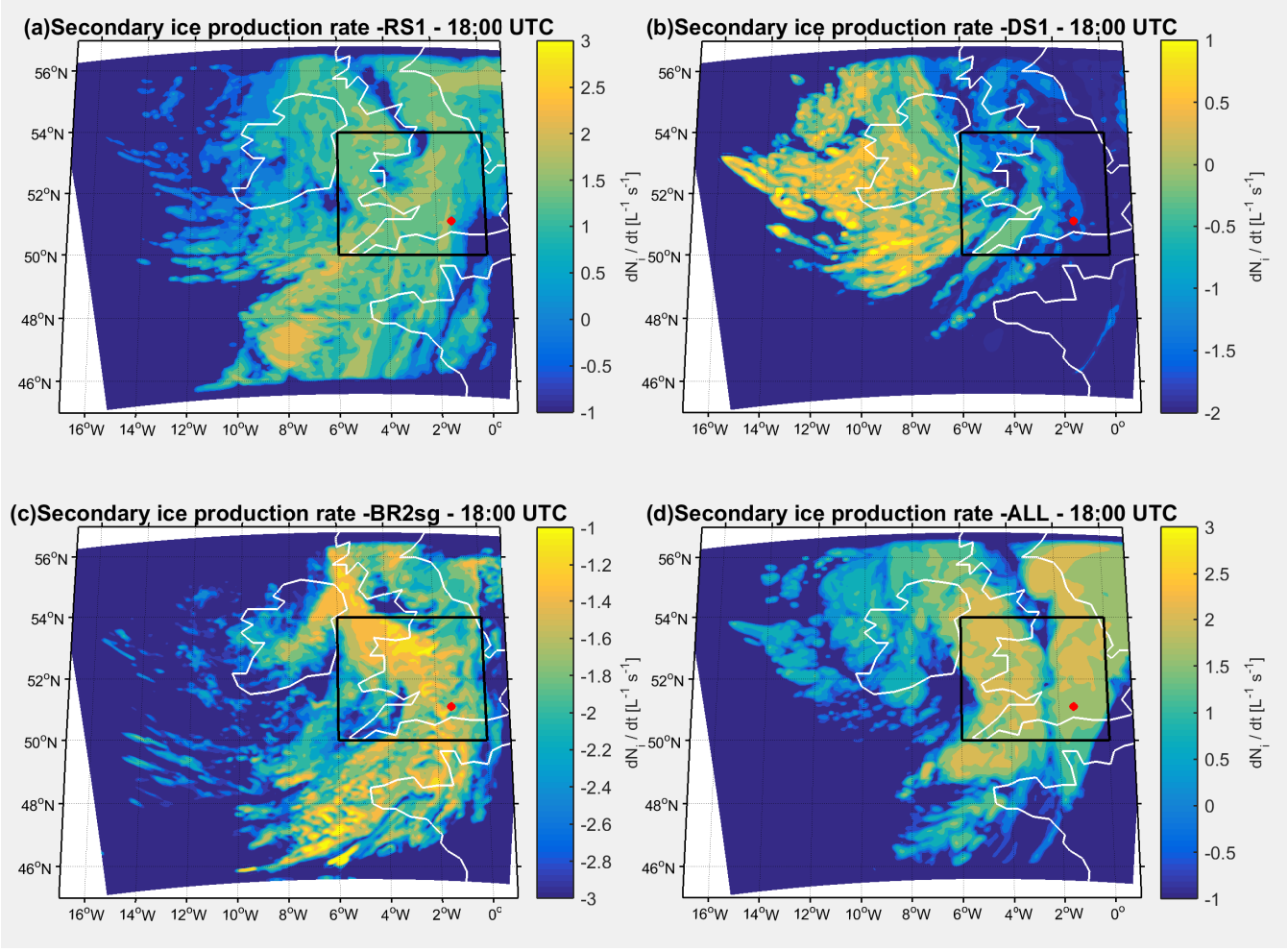

Figure 6. Maps to compare the secondarily-produced ice crystal numbers between 18:00 UTC and 18:30 UTC from (a) rime splintering (RS1 at 3 km) (b) frozen drop shattering (DS1 at 4.5 km) (c) collisional breakup between snow and graupel (BR2sg at 1.5 km) and (d) all secondary processes occurring simultaneously (ALL at 4.5 km). Note the different logarithmic colorbars for each panel. The black box shows the subdomain used in Figure 7, and the red dot is the CFARR location.

Along with these spatial fields, we show the altitudinal, probability, and temporal distributions of modeled and observed ICNC in Figure 7. In panel a, we compare the ~~vertical~~ altitudinal profiles of ICNC ~~in pressure coordinates from 1800 to 2100~~ from 18:00 to 21:00 UTC and in a sub-domain centered at CFARR (49° to 54°N latitude and from 6°W longitude to the Prime Meridian as shown in Figs. 5 and 6). Modeled values were output for ~~pressures from 100 to 900 hPa at 50 hPa intervals , and observations from a clouding~~ altitudes from 1.5 to 7 km hPa with 250 m intervals for the first two and 500 m thereafter. Observations from a cloud imaging probe CIP-15 are discretized into the largest number of ~~pressure~~ altitude bins that still give reliable statistics. IAT algorithms, with those particles below a threshold IAT of 10^{-4} s classified as artifacts, were used to correct the ICNCs Field et al. (2006). No shatter-resistant tips were used on the probe, but given the strict IAT threshold, the possibility of artifacts is limited. The envelopes on all profiles represent the first and third quantiles of ICNC in the interval or bin. Simulated values less than ~~0.01~~ 1 m^{-3} are filtered out.

At the higher altitudes and colder temperatures, the modeled ICNCs all overlap because they use the same representations of heterogeneous and homogeneous ice nucleation. Both the simulated median and standard deviation are also in good agreement with the CIP-15 observations~~. Then at~~ , except for slight underestimations around 6 to 7 km. At the lowest altitudes and warmest temperatures, ~~the 1Ag~~ however, the ALL simulation is the only one ~~to match the observationswell. In fact, the observed and modeled median ICNCs between 800 and 850 hPa are within 30% of one another, indicating the rime splintering process at these warmer subzero temperatures is well-captured by a more generous~~ whose envelope overlaps the observations, both because of the larger rime splintering temperature weighting and ~~fragment number parameter. Inclusion of ice-ice collisional breakup also brings ICNC closer to the observed values in the 3Bg simulation, but the values remain about an order of magnitude too small. The control simulation in red generates by far the fewest crystals, two orders of magnitude less than the observations between 800 and 850 hPa.~~

~~Various distributions of APPRAISE CIP-15 observed and simulated ICNC between 1700 and 2100 UTC for a small domain centered at CFARR with logarithmic scales. Panel a shows altitudinal profiles, where the dotted values indicate median, while the upper and lower envelopes show the first and third quantiles. Panel b shows probability distributions and panel c shows the 30-point running mean time series. Euclidean distance is minimized to find simulated values that correspond to the observed ones in the time series.~~

~~At intermediate altitudes, between 600 and 750 hPa, the observations fall above all the simulated ICNCs, even the upper quantile of the 1Ag simulation. This altitudinal range has a temperature around 258 , where p_{DS} and $\aleph_{BR}$ are maximal, but the underestimation suggests that the parameterizations remain too conservative or that multiple processesare active simultaneously. Indeed,~~ co-occurrence of all secondary production processes. Taylor et al. (2016) also found in their study of cumuli in the same Southwestern Peninsula region ~~, Taylor et al. (2016) find~~ that combinations of secondary production processes ~~are~~ were necessary to explain observed ICNCs. ~~Graupel and hail were not present in large quantities during this case, but a peak in the hydrometeor size profile at 4~~ The importance of the graupel at low levels can also be seen by the high N_i at the lowest level of 1.5 km ~~suggests snow formation there (Crosier et al., 2014). It is also possible then that including snow-snow collisions in Table 1 would bring ICNC into better agreement with the CIP-15 measurements~~(as in Fig. 6c). The underestimated updrafts and radar reflectivities noted above in Section 4.1 may also help explain the too low N_i around 2

km: larger vertical velocities could loft graupel to high altitudes and boost the contribution from collisional breakup. A final contribution to these too low ICNCs may be inclusion of parts of the warm front in the subdomain of analysis.

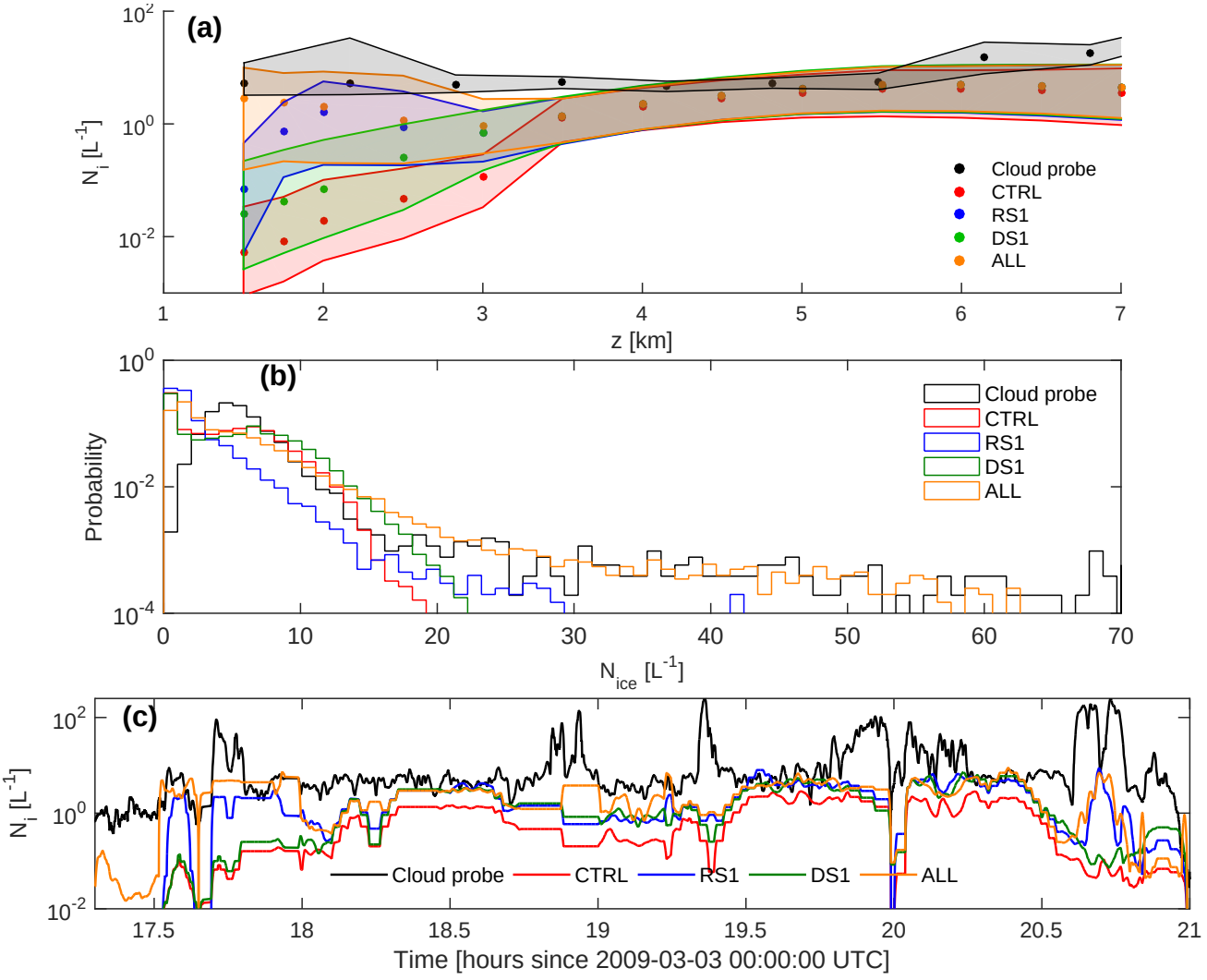

Figure 7. Various distributions of APPRAISE CIP-15 observed and simulated ICNC between 17:00 and 21:00 UTC for a small domain centered at CFARR with logarithmic scales. Panel a shows altitudinal profiles, where the dotted values indicate median, while the upper and lower envelopes show the first and third quantiles. Panel b shows probability distributions and panel c shows the 30-point running mean time series. Euclidean distance is minimized to find simulated values that correspond to the observed ones in the time series.

In panel b, we show the ICNC probability distributions from cloud probe observations (in black) and the ~~control, 1Ag, 3Bg, and 2Big~~ CTRL, RS1, DS1, BR1ig, and ALL simulations (in color) between ~~1800 and 2100~~ 18:00 and 21:00 UTC and between ~~650 and 850 hPa~~1.5 and 3.5 km. Values come again from the subdomain centered at CFARR (shown in black in Figs. 5 and

6). Although the values of less than 10^{-3} L^{-1} have been filtered out, the proability of small N_{ice}, less than 1 L^{-1}, is still much higher for all simulations than observations. At these lower concentrations, however, measurements will be less precise because of sampling volume and flow rate limitations, and model output is more susceptible to numerical noise. The observed distribution is more skewed than the simulated ones with the exception of the ALL simulation: it extends out to N_i of 100 L^{-1} with probabilities of 0.1%. Interestingly, the RS1 simulation that produces the largest $N_{i,sec}$ in the single process simulations (Fig. 6) underestimates the intermediate values of N_i between about 5 and 20 L^{-1}. ~~The simulated and~~

The simulated and observed distributions vary strongly in their higher order moments. The observed distribution is far more skewed with a long tail out to N_{ice} of 100 L^{-1} and has a higher kurtosis as the larger probabilities at low N_{ice} drop off quickly. The simulated distributions drop off more quickly with negligible probabilities by about 45 L^{-1}, and their kurtosis is larger, as the high probabilities at low N_{ice} drop off only slowly through the intermediate values. The ~~probability of small N_{ice}, less than 1 L^{-1} is still much higher in simulations than observations, although values of less than 10^{-3} L^{-1} have been filtered out. At these lower concentrations, however, measurements will be less precise because of sampling volume and flow rate limitations, and model output is more susceptible to numerical noise. The~~ simulation distributions themselves overlap strongly, but differences are present at 35 L^{-1} and above. By concentrations of 45 L^{-1}, only the ~~1Ag and 3Bg~~ RS1 and ALL simulations have non-negligible probabilities. The CTRL simulation is the only one for which all probabilities of N_i greater than 20 L^{-1} are negligible.

Finally, we look at the temporal evolution of N_{ice} in both observations (in black) and the ~~control, 1Ag, 3Bg, and 2Big~~ CTRL, RS1, DS1, and ALL simulations (in color) in panel c. To collocate a simulated value with the observed one at a given time, we use the grid cell that minimizes the Euclidean distance to the latitude, longitude, and altitude where the measurement was made. In some instances then, for example between about ~~1815 and 1835~~ 18:15 and 18:35 UTC, a simulated value is reused because the aircraft circled the same location.Thereafter a thirty-point running mean is calculated for all series. The underestimate in the simulations is apparent again, although it is ~~by far~~ the least for the ~~1Ag~~ ALL simulation, as in the altitudinal profiles of panel a. The observed trends – sudden increases around ~~1730 UTC , right before 1930 UTC, and after 2030~~ 17:30 UTC and after 20:30 UTC or the sudden decrease at ~~2000~~ 20:00 UTC– appear also in the simulated time series. But the ICNC magnitude is always closest to observations in the ~~1Ag simulation with droplet shattering, followed by the 3Bg and 2Big ones with collisional breakup. The control simulation without secondary ice~~ ALL simulation followed by RS1 and then DS1. The CTRL simulation always has the largest discrepancy from cloud probe values. So although simulated ICNC remains too low, the secondary ice parameterizations do consistently shift the values in the right direction.

4.3 Impact on precipitation

Changes in the spatial and temporal distributions of ICNC are expected upon addition of another ice generation mechanism. But the new parameterizations may also have an indirect impact on other metrics. In particular, we consider adjustments to the spatial distributions of accumulated precipitation P_{tot} and of precipitation rate $\dot{P}$. In Figure 8, P_{tot} is shown for a small domain near CFARR at ~~1800 UTC, as the rainband begins to pass~~ 23:30 UTC, after full passage of the rainband over the UK. Panel a shows ~~values from the control~~ P_{tot} from the CTRL simulation, which ~~can already be as high as~~ reaches 30 mm~~in the first~~

~~continental regions over which the rainband passes~~. Larger accumulated rainfall over continental than maritime environments is consistent with observations of other ~~NCFRs~~ narrow cold frontal rainbands (NCFR) (Viale et al., 2013). In panels b through f, deviations from the ~~control simulation field~~ CTRL simulation are shown and are largest in those regions where the magnitude of P_{tot} is ~~largest~~already large. With magnitudes of up to ~~5~~ 10 mm, these deviations represent ~~20~~30% of the signal. ~~Particularly for two small continental regions at (52°N, 4°W) and (51°N, 3°W) and for~~ The sum of the deviations over the whole subdomain is an additional 23.9 m of precipitation for the ~~1Ag~~ RS1 simulation, ~~P_{tot} with secondary iceactive is 20% larger than the control run value~~25.6 m for RS2, 16.9 m for DS1, and 16.6 m for ALL. While the combination of processes generates more ice, it also produces less total precipitation than the secondary prodution processes alone. We emphasize that these P_{tot} deviations are calculated using an average of ~~10~~ 5 ensemble runs, so that the signal reflects the change in microphysics not numerics.

Regions of positive P_{tot} deviation are spatially followed by negative P_{tot} deviation and vice versa. This banding appears in the absolute P_{tot} field of panel a as well and reflects convective structure: vertical motion is strongest in the rainband leading edge, but also preceded and proceeded by ~~weaker convection. Interestingly then~~downdrafts (Fig. 3c). Interestingly, additional ice generation increases the magnitude of these oscillations in convective precipitation. ~~The regionsof upward motion and precipitation generation are enhanced, as are the adjacent downdraft regions. There is a similar patterning in fall streak data from the Doppler radar as well (see Crosier et al. (2014), their Figure 5c)~~ This amplification may be due in part to more riming in the ascending regions, which feeds into precipitation both directly as rimed particles sediment and melt (Fig. 1*(3)*) and indirectly as they splinter and generate more rimable particles (Fig. 1*(4)*). Higher concentrations of rimed particles would be in line with the higher values of differential reflectivity at the convective cloud top, noted by Crosier et al. (2014). Orography in this region also has an impact. The spot of particularly large P_{tot} around 50.5°N and 4°W corresponds to the Dartmoor with a maximum elevation of 621 m. Slightly elevated P_{tot} is also present over the Exmoor and Bodmin Moor at (51°N, 3.5°W) and (50.5°N, 4.5°W) respectively.

As in Figure 5, the impact of adjusting ~~$\aleph_{RS}$~~ w_{RS} can be seen here between ~~1Ag~~ RS1 in panel b and ~~1Ac in panel f. The fragment number parameter shifts the magnitude rather than the spatial distribution of the deviations. Regions of positive versus negative deviation overlap, but are about two times larger in magnitude for the 1Ag simulationthan the 1Ac one. This result favors the red pathway~~ RS2 in panel c. The increased temperature weighting actually reduces the magnitude of ΔP_{tot} in some regions for the RS2 simulation. As in the ALL simulation above, this could be due to the kind of 'cloud lifetime effect' shown in Figure 1~~, whereby the Bergeron process activates at higher ICNC and lower supersaturation and grows crystals to sedimentable size. A final point is that the deviations are not so different between the simulations with droplet shattering in panels b, e, and f and those with ice-ice collisional breakup in panels c and d, suggesting that rime splintering is responsible for much of the change~~ *(1)* in which many small ice crystals do not sediment as quickly. Deviations in the DS1 precipitation are concentrated in a single band and are reduced over the continent where the large droplets are less numerous relative to those from the RS* simulations. The largest changes in P_{tot} are actually due to modest rime splintering.

Deviations in $\dot{P}$ (Fig. S2) exhibit much of the same behavior as the P_{tot} field. The highest and lowest deviations ~~fall along the comma shaped curve of the rainband, apparent also in Figure 5. The P_{tot} 'hotspots' at (52°N, 4°W) and (51°N, 3°W) mentioned above reappear, but~~ align almost exactly with the most extreme low-level updrafts (3). 'Hotspots' appear again in

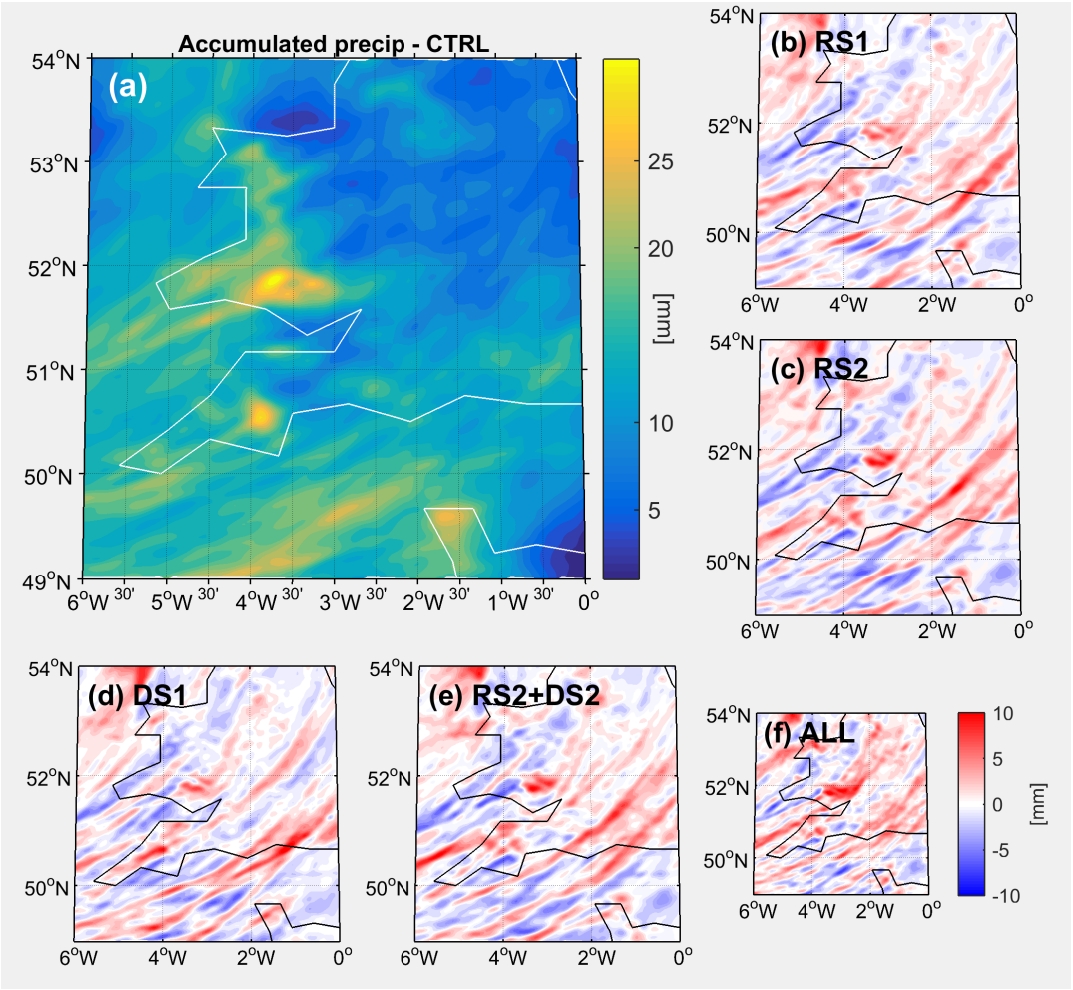

Figure 8. Panel a shows the spatial distribution of accumulated precipitation in the control simulation for a small domain near CFARR at ~~1800~~ 23:30 UTC, ~~as~~ after full passage of the rainband ~~begins to pass~~ over the UK. Panels b though f show the deviations of accumulated precipitation in five of the simulations with the secondary ice parameterizations in place.

the P_{tot} field with 'coldspots' in between. ~~These spots are the result of an NCFR structure with~~ Here the impact of the updraft structures is even more evident, with the 'hotspots coincident with cores of convective precipitation ~~surrounded by more stable areas called~~ in the NCFR and surrounding 'coldspots' coincident with its more stable gap regions (James and Browning; Hobbs and Persson, 1982; Crosier et al., 2014). The addition of the secondary ice parameterizations both invigorates the precipitation in the convective regions and ~~corresponding precipitation and strengthens the gap downdrafts and corresponding drying . Increasing the fragment number $\aleph_{RS}$ from 1Ac to 1Ag enhances these effects again, and the largest deviations again occur over the continents and due to rime splintering.~~ strengthens the corresponding drying in adjacent gap regions.

Finally in Figure 9, we show the simulated and observed time series of precipitation rate in color and black respectively for the same domain near CFARR between ~~1700 and 2200~~ 17:00 and 22:00 UTC. Observations come from the Met Office C-band NIMROD System of rain radars at 5 km spatial and 15 min temporal resolution. The domain-mean values and standard deviation envelopes are shown for both. In panel a, the standard deviation of mean values in a 1~~degree longitude-1degree~~ ° longitude-1° latitude box (1-2°W, 51-52°N) around CFARR is used, whereas in panel b, the mean standard deviation over the ~~10-simulation~~ 5-simulation ensemble is used. The first can be understood as spatial variance and the second as numerical, and the first is much larger. Because the rainband is so narrow, this is especially true at later times during its passage: the intense precipitation may extend over only 10 kilometers or less, while the small domain around CFARR is still about 50 kilometers by 50 kilometers. In neither case does the evolution of the mean $\dot{P}$ for different simulations vary significantly from one to the next.

Spatial variance aside, the simulations do not capture the rainband narrowness well in the time series. There is a broad increase in precipitation rate from about ~~1900 UTC through 2100~~ 19:00 UTC through 21:00 UTC, but not the sharp increase to 40 mm h^{-1} as in the observations. The simulations reproduce at most 75% of the magnitude of the maximum $\dot{P}$ ~~and all~~ but tend to fall within the spread of ~~one another~~the observations. This similarity of the simulated series upon spatial averaging may be expected because of the finer-scale rainband structure discussed above, but the averaging is retained for a more robust trend. And in spite of this, the mean $\dot{P}$ remains closest to the observations in the ~~1Ac and 1Ag simulations with droplet shattering~~RS2 simulation, followed by the ~~3Bg and 2Big oneswith collisional breakup, and lastly the control simulation. This 'hierarchy' of simulations is the same as for ICNCs from Figure 7c.~~ RS1 and DS1 ones.

5 Discussion

~~From the time series of N_{ice} in Figure 7, we can estimate secondary ice production rates (Fig. **??**). The rates calculated from simulated N_{ice} vary widely, even with extensive smoothing, because the time series constructed in Figure 7 uses the value closest in space and time to the observations and hence often has plateaus of the same N_{ice}. Nevertheless, we can get an order-of-magnitude estimate with a simple finite difference, and the rates from observations are relatively more continuous with smoothing.~~

~~From the 1Ag simulation, quite high production rates of up to 50 L^{-1} s^{-1} are generated over periods of 5 to 10 minutes early on. The other simulations produce maximum rates of 5 L^{-1} s^{-1} around 1930 and 2000 UTC, while the observations produce~~

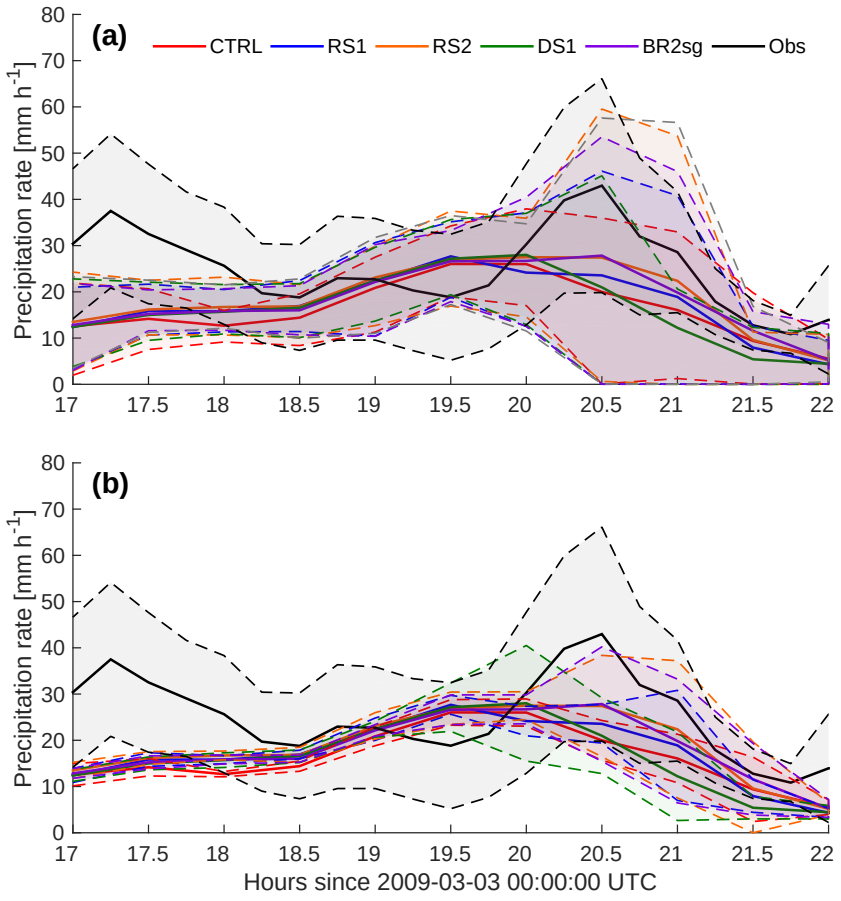

Figure 9. Time series of precipitation rate, both from the UK NIMROD rain radar in black and from various simulations in color for a small domain around CFARR from ~~1700~~ 17:00 to ~~2200~~ 22:00 UTC. For all traces, the mean is shown with an envelope of plus-minus a standard deviation for the observations and the first and third quantile for the simulations. In panel a, the ~~standard deviation is~~ quantiles are calculated over the small spatial domain, and in panel b, ~~the standard deviation is~~ they are calculated over the ~~10-member~~ 5-member ensemble.

~~up to 2.5 L^{-1} s^{-1} around 1920 UTC. When there is no spatial averaging as in Figure 5, production rates from secondary ice production alone are as high as 25 L^{-1} s^{-1} (10^5 L^{-1} h^{-1}) in certain regions. Outside a few peaks in ice generation , the production rate stays around 10^{-2} L^{-1} s^{-1}. If the observed peak production rate of 2.5 L^{-1} s^{-1} lasts for 2 minutes, it will generate an ICNC of 300 L^{-1}. And if we assume a sedimentation rate of 10^{-6} g ice (kg air)$^{-1}$ s^{-1}, equivalent to about 0.25 L^{-1} s^{-1} for small crystals, the cloud will last for 20 minutes thereafter. If the air is not quiescent, the peak production could be reinvigorated and the lifetime elongated~~Additional ice generation in different regions, as shown in Figures 5 and 6, will have energetic implications. First many small ice crystals are more likely to be advected into a convective outflow region where they will contribute to cirrus optical thickening and resultant surface warming. As mechanical processes, rime splintering and collisional breakup do not have direct latent heating effects; however, droplet riming becomes more likely in the presence of higher ICNCs, creating an 'indirect latent heating effect'. For droplet shattering, the phase change as the raindrop freezes releases heat of fusion and may invigorate the surrounding updrafts. More latent heating aloft can intensify the upper-level anticyclonic potential vorticity (PV) (Willison et al., 2013). This PV generation may suppress further cyclogenesis by disconnecting the developing system from surface potential temperature anomalies. On the other hand, higher cyclonic diabatic PV may slow system progression and maintain favorable levels of shear. Freezing should also intensify detrainment, as shown in the modeling sensitivity studies of Sud and Walker (2003). In these mechanisms, ice crystal production can be a mediator of circulation-radiation feedbacks.

~~The calculated production rates from observations tend to be in agreement with other values in the literature, while those from the simulations are on the high side. Based upon measurements taken over Montana, California, and Florida, Harris-Hobbs and Cooper (198 estimated ice production rates in cumulus clouds with a difference in ICNC at two sizes normalized by the growth time between those sizes. The majority of their measured and predicted production rates fell between 0.001 and 0.1 L^{-1} s^{-1}, although their probes were probably subject to shattering artifacts (Field et al., 2017). Using the same methodology, Taylor et al. (2016) calculate ice production rates of 0.11 L^{-1} s^{-1} in a dynamic mixed-phase cloud over the southwestern United Kingdom with up- and downdrafts in the $\pm$3 m s^{-1} range and ICNC around 50 L^{-1}. For a more quiescent and glaciated cloud, with updrafts of about 1 m s^{-1} and ICNC up to 270 L^{-1}, they calculate a slightly higher production rate of 0.14 L^{-1} s^{-1}. Mossop (1976) observed ice production rates of 100 s^{-1} at 1.8 m s^{-1} and 200 at 2.4 m s^{-1}, both at -5°C in their cubic meter cloud chamber.Despite these lower production rates, these lasted for as long as 30 minutes.~~ Variations of aerosol concentration and surface radiative budget over continent versus ocean should also affect the efficiency of these processes. As aerosol loadings increase over continental regions, more and smaller cloud droplets form for a fixed cloud liquid water content. This shift in the droplet size distribution will diminish the riming and droplet freezing efficiencies. In this case, however, without moisture limitations and only a narrow continental region, no notable land-sea differences appear in our spatial snapshots (e.g., Fig. 5).

From Figures 5 and 6, the model can generate 1000 crystals per liter per half hour by secondary production. In mixed-phase parcel model simulations, we have ~~also~~ calculated slower but longer-lasting secondary ice production rates than in these mesoscale simulations (Sullivan et al., 2017, 2018). In simulations that include rime splintering and ice-ice collisional breakup, the model generates about ~~0.001~~ 1 to 10 L^{-1} ~~s~~(half hour)$^{-1}$ even when a description of ice non-sphericity is included. ~~But again, these rates last for much longer than those shown in Figure **??**, up to 20 minutes. This dichotomy of larger, shorter-lived~~

~~and smaller, longer-lived~~ Larger production rates in ~~different simulations~~ the mesoscale model can be attributed in part to the representation of the largest hydrometeors, which are crucial both to secondary ice production and precipitation processes. The parcel model contains only six size bins and so does not capture the tail of the size distribution present in the COSMO simulations. Inclusion of hydrometeor number from these tails will enhance the ~~secondary ice production rates, i.e. the~~ tendencies in Equations 1, 4, and 7. But it also enhances the sedimentation rates, so that that multiplication feedbacks (like that shown in green in Figure 1) will be limited in their efficiency.

We have also used parcel model simulations to comment on the relative importance of droplet shattering and ice-ice collisional breakup. Sullivan et al. (2017) found that the dominance of rime splintering versus collisional breakup was determined by timing of large hydrometeor formation in the liquid versus ice phase. Given the relatively low graupel and hail numbers for this cold frontal rainband (Crosier et al., 2014), it is to be expected then that the rime splintering parameterization is most influential on P_{tot} (Section 4.3). The analogous $N_{i,sec}$ field for ice-ice collisional breakup (Figure ~~??~~6c) is about ~~two~~ four orders of magnitude less than those ~~shown for droplet shattering in Figure 5~~for rime splintering (Figure 5). These lower magnitudes reflect to some extent the "self-limiting nature" of ice-ice collisional breakup as well because ice hydrometeors must be consumed to generate them in this process. ~~The absence of a defined rainband structure in Figure ?? corroborates the idea of Sullivan et al. (2018) that secondary ice production processes involving the liquid phase rely more heavily on dynamical "sweet spots" than those involving just the ice phase. Higher~~ Localized enhancement and dynamical dependence of ~~the processes involving the liquid phase~~ these secondary production processes should be even more ~~true~~ evident for simulations at higher spatial resolutions: convection would be better resolved and higher liquid water contents would be generated.

The spatiotemporal resolution, along with the microphysics scheme, also plays into the strong feedbacks between hydrometeor formation, latent heating, and cloud dynamics. Previous studies have generally found a spatial resolution of 4 to 6 km to be sufficient to reproduce precipitation extremes (e.g. Prein et al., 2013; Pieri et al., 2015). This resolution dependence results from changes in the vertical moisture advection, in turn due to adjustments of vertical velocity with resolution (Yang et al., 2014). For simulations whose resolutions border on the "gray zone" scales (around a tenth of a degree), over-representation of convective activity is possible by both the parameterization and explicit resolution (Pieri et al., 2015); however, our simulations are at a fully convection-permitting scale and use only a reduced form of the Tiedtke mass-flux scheme for shallow convection (Tiedtke, 1989) and this should not be a concern.

The use of a two-moment scheme is also important for simulation of extreme precipitation (Otkin et al., 2006). Certain one-moment schemes tend to generate overly large drops and too high precipitation rates (Thompson et al., 2004), but SB06 tends to produce especially large quantities of graupel (Otkin et al., 2006). The Bigg parameterization, as a precursor to our droplet shattering additions, has been shown in previous studies to predict very low numbers of frozen drops (e.g. Morrison et al., 2005; Fan , which may contribute to underestimation of its contribution here. The more rigorous alternative would be to account for immersed surface area and scavenging of ice nucleating particles as in Paukert and Hoose (2014); Paukert et al. (2017), and future work should implement an updated immersion freezing parameterization.

6 Summary

New frozen droplet shattering and ice-ice collisional breakup parameterizations have been developed and implemented into the regional COSMO weather model. We performed several simulations of a cold frontal rainband, observed during the APPRAISE campaign over the UK, with adjustments to the new parameterization formulations. With these runs, we have shown the following:

1. *ICNC generated by secondary production processes can be as large as those from primary nucleation, ~~but~~ especially in ~~limited domains near~~ the presence of sufficient convective ~~leading edges where large hydrometeors are present~~activity and rain, snow, or graupel mixing ratios.*

   The new parameterizations calculate $N_{i,sec}$ production rates of up to ~~10^5~~ 1000 L^{-1} per half hour, values on the order of the primary nucleation tendency ~~, in localized regions. These localized regions~~ at certain altitudes. The localized regions of large secondary ice production are characterized by convective updrafts and by optimal temperatures that maximize parameters like ~~N_{BR}~~ w_{BS} or p_{DS}. The role of the convective updraft is two-fold, both to generate a supersaturation that forms and grows ~~a large hydrometeor~~ large hydrometeors and then to loft ~~that hydrometeor~~ those to the optimal temperature zone. In this case, we saw that rime splintering was the most important process in line with the conclusions of Crosier et al. (2014); however, underestimation of vertical velocities in the cold front also led to underestimation in simulated radar reflectivity relative to observations. If this Z_{DH} difference was caused by additional graupel at higher altitudes, contributions from collisional breakup could have been much higher than the 0.1 L^{-1} per half hour found here. A low bias in updrafts also generates fewer raindrops at altitude and limits the contribution from frozen droplet shattering (in this case to an intermediate production rate of 10 L^{-1} per half hour).

2. *ICNCs greater than 50 L^{-1} are ~~still significantly~~ underestimated with the addition of single secondary production parameterizations.*

   ~~From altitudinal profiles, these underestimates are concentrated~~ Generally, the addition of secondary ice parameterizations moves the ICNC magnitudes in both vertical and temporal distributions toward the observed values, but underestimates persist, particularly at altitudes between about 2 and 4 km~~, where the secondary production processes should be active~~. In time series, sudden increases or decreases in ICNC are well-captured but their magnitude remains about an order of magnitude too small. The combination of processes ~~or~~ in the ALL simulation does the best in reproducing the observed histogram and time series, but a feedback between ~~them may~~ the processes may still be missing in the current formulations~~, or fragment number parameters may be underestimated, although the latter seems unlikely from laboratory estimates. Nonetheless, addition of the secondary ice parameterizations moves the ICNC magnitudes in both vertical and temporal distributions toward the observed values .~~. Underestimations stem in part from low biases in the updraft velocity. If the vertical velocities can be brought into agreement with observations, then criteria in these values as well as temperature could be used together to parameterize secondary production in appropriate thermodynamic zones. For two-moment schemes, graupel, snow, and raindrop criteria could be implemented for these processes

3. *The variation between convective precipitation regions and neighboring quiescent ones is intensified by the addition of secondary ice production.*

The addition of secondary ice systematically increases accumulated precipitation or precipitation rate in regions where these values are largest. The magnitude of these increases can be up to ~~20~~30% of the signal, ~~but again is very localized~~ again in very localized regions, and reduction in P_{tot} and $\dot{P}$ occur in adjacent gap regions. ~~The same effect occurs in both the droplet shattering and ice-ice collisional breakup simulations, meaning that~~ For this particular case, rime splintering is the most influential process for precipitation formation~~in this particular case. Adjustments in fragment number do not alter the spatial distribution of the effect, only its magnitude~~, and interestingly, widening its temperature weighting actually weakens the positive anomalies of P_{tot} in a kind of 'cloud lifetime effect' whereby additional small ice generation lengthens cloud duration. Inclusion of secondary ice parameterizations ~~also brings~~ does not bring the simulated maximum precipitation intensity much closer to the observed value, ~~although this change is less pronounced and the maximum $\dot{P}$ is still underestimated by 25%~~and the narrowness of the rainband is still not well-reproduced.

7 Code availability

Documentation of the updates to SB06, the Seifert and Beheng two-moment scheme within the larger COSMO model, ice-ice collisional breakup subroutines, and NetCDF4 output files from sensitivity tests are all available upon request.

8 Data availability

The UK 1 km-resolution NIMROD radar data are available through the Met Office Centre for Environmental Data Analysis at http://catalogue.ceda.ac.uk/uuid/82adec1f896af6169112d09cc1174499. Filtered CIP-15 ICNC data from the 3 March 2009 flight are available upon request, and their corresponding latitude, longitude, and altitudes are available through CEDA at http://data.ceda.ac.uk/badc/faam/data/2009/b433-mar-03/core_processed.

Appendix A: Rain freezing parameterization

Within the Seifert and Beheng two-moment scheme, the number of freezing droplets is calculated with the stochastic model of Bigg (1953):

$$\ln(1 - P_{freez}) = -\int_0^t V_R J_{het} dt, \tag{A1}$$

$$= -\frac{\pi}{6} \int_0^t D_R^3 J_{het} dt \tag{A2}$$

where the heterogeneous nucleation coefficient is defined as $J_{het} = b_{het}\exp(a_{het}\Delta T - 1)$ and ΔT is the supercooling. We use a_{het} of 0.65 and b_{het} of 200 as in Barklie and Gokhale (1959). Then the number of freezing droplets per time is given by

$$\frac{\partial N_{freez}}{\partial t} = -N_R \bar{x}_R J_{het} \tag{A3}$$

where N_R is the raindrop number and $\bar{x}_R$ is the mean mass per raindrop.

Appendix B: Hydrometeor size distributions and collision integrals

The generalized Γ size distribution is used for the hydrometeor size distributions within the Seifert and Beheng two-moment scheme:

$$f(x) = Ax^{\nu}\exp(-\lambda x^{\mu}) \tag{B1}$$

where $(\nu+1)/\mu$ is the shape parameter, λ the rate parameter of the distribution, and x is hydrometeor mass. Then the number of particles of type j that are collected by type k is given by

$$\left.\frac{\partial N_j}{\partial t}\right|_{coll,jk} = -\int_0^{\infty}\int_0^{\infty} f_j(x_j) f_k(x_k) K_{jk}(x_j, x_k) dx_j dx_k \tag{B2}$$

where K_{jk} is the collection kernel, the product of the collisional cross section, a collection efficiency, and a differential settling velocity:

$$K_{jk}(x_j, x_k) = \frac{\pi}{4}[D_j(x_j) + D_k(x_k)]^2 E_{jk}(x_j, x_k)|v_j(x_j) - v_k(x_k)| \tag{B3}$$

To obtain the analytical expression for the collision integral in Equation 6, the collection efficiency is assumed to be independent of particle sizes: $E_{jk}(x_j, x_k) \approx \overline{E_{jk}}$. The particle diameter is assumed to relate to particle mass through a power law expression: $D_j(x_j) = a_j x_j^{b_j}$. And the differential settling velocity is approximated by a characteristic difference: $|v_j(x_j) - v_k(x_k)| \approx \overline{\Delta v_{jk}}$. Then Equation B2 becomes

$$\left.\frac{\partial N_j}{\partial t}\right|_{coll,jk} = -\frac{\pi}{4}\overline{E_{jk}}\,\overline{\Delta v_{jk}}\int_0^{\infty}\int_0^{\infty} f_j(x_j) f_k(x_k)[D_j(x_j) + D_k(x_k)]^2 dx_j dx_k \tag{B4}$$

Wisner et al. (1972) have solved this equation with the non-dimensional values δ and θ given by

$$\delta_j^{\kappa} = \frac{\Gamma(\frac{2b_j+\nu_j+1+\kappa}{\mu_j})}{\Gamma(\frac{\nu_j+1}{\mu_j})}\left[\frac{\Gamma(\frac{\nu_j+1}{\mu_j})}{\Gamma(\frac{\nu_j+2}{\mu_j})}\right]^{2b_j+\kappa} \qquad \theta_j^{\kappa} = \frac{\Gamma(\frac{2\beta_j+2b_j+\nu_j+1+\kappa}{\mu_j})}{\Gamma(\frac{2b_j+\nu_j+1+\kappa}{\mu_j})}\left[\frac{\Gamma(\frac{\nu_j+1}{\mu_j})}{\Gamma(\frac{\nu_j+2}{\mu_j})}\right]^{2\beta_j} \tag{B5}$$

These non-dimensional values and their derivation are given in greater detail in Seifert (2002) and Seifert and Beheng (2006).

Appendix C: Notation

γ Decay rate in the fragment number generated from ice-ice collisional breakup

λ Rate parameter in the generalized Γ distribution

μ**,** ν Factors within the shape parameter of the generalized Γ distribution

σ Standard deviation in the raindrop shattering probability distribution function

ICNC In-cloud ice crystal number concentration

INP Ice-nucleating particle number

$N_{i,pri}$ Primarily nucleated ice crystal number concentration

$N_{i,sec}$ Secondarily produced ice crystal number concentration

N_R Raindrop number

$\aleph_{BR}$ Fragment number from ice-ice collisional breakup per collider (e.g., graupel in *ig or *sg simulations) number

$\aleph_{DS}$ Fragment number from droplet shattering per large droplet number

$\aleph_{RS}$ Fragment number from rime splintering per milligram of rime

p_{DS} Temperature dependent probability that a freezing raindrop shatters

P_{freez} Probability that a raindrop freezes versus time according to Bigg (1953)

p_{max} Maximum probability that a freezing raindrop shatters, parameter within p_{DS}

$\dot{P}$ Precipitation intensity

P_{tot} Accumulated precipitation

T_{min} Minimum temperature for ice-ice collisional breakup to occur

T_{μ} Associated temperature for the maximum in the raindrop shattering probability distribution function

V_R Raindrop volume

$\overline{x_R}$ Mean raindrop mass

Author contributions. SCS and CH constructed the parameterizations and chose the case study. SCS implemented the parameterizations in COSMO. CB and IZ assisted with model setup and porting, and JC provided campaign data and analysis codes. SCS, CH, and AN analyzed simulation output. All authors reviewed the writing.

Competing interests. The authors declare that they have no conflict of interest.

Acknowledgements. The comments of two anonymous reviewers have substantially improved our analyses. SCS and CH thank support from the Helmholtz Association through the President's Initiative and Networking Fund (VH-NG-620). SCS and AN acknowledge funding from a NASA Earth and Space Science Fellowship (NNX13AN74H) and NASA MAP grant, as well as the DOE EaSM. JC and the source campaigns for our data were funded by the NERC APPRAISE programme, grant number NE/E01125X/1. All authors wish to thank the Deutscher Wetterdienst (DWD) for providing the COSMO model code as well as the initial and boundary data. In addition, SCS would like to thank Marco Paukert, Isabelle Reichardt, Tobias Schad, Heike Vogel, and Luke Hande for helpful discussion about the COSMO model during a six-month stay at the Institute of Meteorology and Climate Research in Karlsruhe.

References

Aleksić, N.: Precipitation effects of hail suppression in Serbia, Theor. Appl. Climatol., 40, 271–279, doi:10.1007/BF00865978, 1989.

Arkin, P. A. and Meisner, B. N.: The relationship between large-scale convective rainfall and cold cloud over the Western Hemisphere during 1982-84, Mon. Weather Rev., 115, 51–74, doi:10.1175/1520-0493(1987)115<0051:TRBLSC>2.0.CO;2, 1987.

Baldauf, M., Seifert, A., Förstner, J., Majewski, D., and Raschendorfer, M.: Operational convective-scale numerical weather prediction with the COSMO model: Description and sensitivities, Mon. Weather Rev., 139, 3887–3905, doi:10.1175/MWR-D-10-05013.1, 2011.

Barahona, D., Rodriguez, J., and Nenes, A.: Sensitivity of the global distribution of cirrus ice crystal concentration to heterogeneous freezing, J. Geoph. Res., 115, doi:10.1029/2010JD014273, 2010.

Barklie, R. H. D. and Gokhale, N.: The freezing of supercooled water drops, 1959.

Bigg, E. K.: The formation of atmospheric ice crystals by the freezing of droplets, Q. J. Roy. Meteorol. Soc., 79, 510–519, doi:10.1002/qj.49707934207, 1953.

Broadley, S., Murray, B., Herbert, R., Atkinson, J., Dobbie, S., Malkin, T., Condliffe, E., and Neve, L.: Immersion mode heterogeneous ice nucleation by an illite rich powder representative of atmospheric mineral dust, Atmos. Chem. Phys., 12, 287–307, doi:10.5194/acp-12-287-2012, 2012.

Buizza, R., Milleer, M., and Palmer, T. N.: Stochastic representation of model uncertainties in the ECMWF ensemble prediction system, Quar. Jour. Roy. Meteor. Soc., 125, 2887–2908, doi:10.1002/qj.49712556006, 1999.

Choularton, T. W., Griggs, D. J., Humood, B. Y., and Latham, J.: Laboratory studies of riming, and its relation to ice splinter production, Quart. J. Roy. Meteor. Soc., 106, 367–374, doi:10.1002/qj.49710644809, 1980.

Clark, P., Choularton, T. W., Brown, P. R. A., Field, P. R., Illingworth, A. J., and Hogan, R. J.: Numerical modelling of mixed-phase frontal clouds observed during the CWVC project, Q. J. R. Meteorol. Soc., 131, 1677–1693, doi:10.1256/qj.03.210, 2005.

Connolly, P., Heymsfield, A. J., and Choularton, T. W.: Modelling the influence of rimer surface temperature on the glaciation of intense thunderstorms: The rime-splinter mechanism of ice multiplication, Q. J. Roy. Meteorol. Soc., 132, 3059–3077, doi:10.1256/qj.05.45, 2006a.

Connolly, P. J., Choularton, T. W., Gallagher, M. W., Bower, K. N., Flynn, M. J., and Whiteway, J. A.: Cloud-resolving simulations of intense tropical *Hector* thunderstorms: Implications for aerosol-cloud interactions, Q. J. Meteorol. Soc., 132, 3079–3106, doi:10.1256/qj.05.86, 2006b.

Crawford, I., Bower, K. N., Choularton, T. W., Dearden, C., Crosier, J., Westbrook, C., Capes, G., Coe, H., Connolly, P. J., Dorsey, J. R., Gallagher, M. W., Williams, P., Trembath, J., Cui, Z., and Blyth, A.: Ice formation and development in aged, wintertime cumulus over the UK: observations and modelling, Atmos. Chem. Phys., 12, 4963–4985, doi:10.5194/acp-12-4963-2012, 2012.

Crosier, J., Choularton, T. W., Westbrook, C. D., Blyth, A. M., Bower, K. N., Connolly, P. J., Dearden, C., Gallagher, M. W., Cui, Z., and Nicol, J. C.: Microphysical properties of cold frontal rainbands, Q. J. Roy. Meteorol. Soc., 140, 1257–1268, doi:10.1002/qj.2206, 2014.

Curry, J. A. and Khvorostyanov, V. I.: Assessment of some parameterizations of heterogeneous ice nucleation in cloud and climate models, Atmos. Chem. Phys., 12, 1151–1172, doi:10.5194/acp-12-1151-2012, 2012.

Dearden, C., Vaughan, G., Tsai, T., and Chen, J.: Exploring the diabatic role of ice microphysical processes in two North Atlantic summer cyclones, Mon. Wea. Rev., 144, 1249–1272, doi:10.1175/MWR-D-15-0253.1, 2016.

DeMott, P. J., Prenni, A. J., Liu, X., Kreidenweis, S. M., Petters, M. D., Twohy, C. H., Richardson, M. S., Eidhammer, T., and Rogers, D. C.: Predicting global atmospheric ice nuclei distributions and their impacts on climate, Proc. Nat. Acad. Sci., doi:10.1073/pnas.0910818107, 2010.

DeMott, P. J., Hill, T. C. J., McCluskey, C. S., Prather, K. A., Collins, D. B., Sullivan, R. C., Ruppel, M. J., Mason, R. H., Irish, V. E., Lee, T., Hwang, C. Y., Rhee, T. S., Snider, J. R., McMeeking, G. R., Dhaniyala, S., Lewis, E. R., Wentzell, J. J. B., Abbatt, J., Lee, C., Sultana, C. M., Ault, A. P., Axson, J. L., Martinez, M. D., Venero, I., Santos-Figueroa, G., Stokes, M. D., Deane, G. B., Mayol-Bracero, O. L., Bertram, V. H. G. T. H., Bertram, A. K., Moffett, B. F., and Franc, G. D.: Sea spray aerosol as a unique source of ice nucleating particles, Proc. Natl. Acad. Sci., 113, 5797–5803, doi:10.1073/pnas.1514034112, 2016.

Doms, G. and Baldauf, M.: A description of the nonhydrostatic regional COSMO-Model. Part II: Physical parameterization, Tech. rep., 2015.

Fan., J., Ovtchinnikov, M., Comstock, J. M., McFarlane, S. A., and Khain, A.: Ice formation in Arctic mixed-phase clouds: Insights from a 3-D cloud-resolving model with size-resolved aerosol and cloud microphysics, J. Geophys. Res., 114, doi:10.1029/2008JD010782, 2009.

Field, P., Lawson, P., Brown, G., Lloyd, C., Westbrook, D., Moisseev, A., Miltenberger, A., Nenes, A., Blyth, A., Choularton, T., Connolly, P., Bühl, J., Crosier, J., Cui, Z., Dearden, C., DeMott, P., Flossmann, A., Heymsfield, A., Huang, Y., Kalesse, H., Kanji, Z., Korolev, A., Kirchgaessner, A., Lasher-Trapp, S., Leisner, T., McFarquhar, G., Phillips, V., Stith, J., and Sullivan, S.: Chapter 7: Secondary ice production - current state of the science and recommendations for the future, Meteor. Monogr., doi:10.1175/AMSMONOGRAPHS-D-16-0014.1, 2017.

Field, P. R., Wood, R., Brown, P. R. A., Kaye, P. H., Hirst, E., Greenaway, R., and Smith, J. A.: Ice particle interarrival times measured with a fast FSSP, J. Atm. Ocean. Tech., 20, 249–261, doi:10.1175/1520-0426(2003)020, 2003.

Field, P. R., Heymsfield, A. J., and Bansemer, A.: Shattering and particle interarrival times measured by optical array probes in ice clouds, J. Atm. Ocean. Tech., 23, 1357–1371, doi:10.1175/JTECH1922.1, 2006.

Glassmeier, F. and Lohmann, U.: Constraining precipitation with susceptibility of warm-, ice-, and mixed-phase clouds with microphysical equations, J. Atm. Sci., 73, 5003–5023, doi:10.1175/JAS-D-16-0008.1, 2016.

Hallett, J. and Mossop, S. C.: Production of secondary ice particles during the riming process, Nature, 249, 26–28, doi:10.1038/249026a0, 1974.

Harris-Hobbs, R. L. and Cooper, W. A.: Field evidence supporting quantitative predictions of secondary ice production rates, J. Atmos. Sci., 44, 1071–1082, doi:10.1175/1520-0469(1987)044<1071:FESQPO>2.0.CO;2, 1987.

Heymsfield, A. and Willis, P.: Cloud conditions favoring secondary ice particle production in tropical maritime convection, 71, 4500–4526, doi:10.1175/JAS-D-14-0093.1, 2014.

Heymsfield, A. J.: On measurements of small ice particles in clouds, Geophys. Res. Lett., 34, doi:10.1029/2007GL030951, 2007.

Heymsfield, A. J. and Mossop, S. C.: Temperature dependence of secondary ice crystal production during soft hail growth by riming, Q. J. Roy. Meteorol. Soc., 110, 765–770, doi:10.1002/qj.49711046512, 1984.

Hobbs, P. V. and Persson, P. O. G.: The mesoscale and microscale structure and organization of clouds and precipitation in midlatitude cyclones. Part V: the substructure of narrow cold-frontal rainbands, J. Atm. Sci., 39, 280–295, doi:10.1175/1520-0469(1982)<0280:TMAMSA>2.0.CO;2, 1982.

Hoose, C. and Möhler, O.: Heterogeneous ice nucleation on atmospheric aerosols: a review of results from laboratory experiments, Atmos. Chem. Phys., 12, 12 531–12 621, doi:10.5194/acpd-12-12531-2012, 2012.

James, P. K. and Browning, K. A.: Mesoscale structure of line convection at surface cold fronts, Q. J. R. Meteorol. Soc., 105, 371–382, doi:10.1002/qj.4971054404.

Joyce, R. and Arkin, P. A.: Improved estimates of tropical and subtropical precipitation using the GOES precipitation index, J. Atm. Ocean. Tech., 14, 997–1011, doi:10.1175/1520-0426(1997)014<0997:IEOTAS>2.0.CO;2, 1997.

Khain, A., Rosenfeld, D., and Pokrovsky, A.: Aerosol impact on the dynamics and microphysics of deep convective clouds, Q. J. R. Meteorol. Soc., 131, 2639–2663, doi:10.1256/qj.04.62, 2005.

Knopf, D. A. and Koop, T.: Heterogeneous nucleation of ice on surrogates of mineral dust, J. Geophys. Res., 111, doi:10.1029/2005JD006894, 2006.

Korolev, A.: A study of bimodal droplet size distributions in stratiform clouds, Atm. Res., 32, 143–170, doi:10.1016/0169-8095(94)90057-4, 1994.

Korolev, A.: Limitations of the Wegener-Bergeron-Findeisen mechanism in the evolution of mixed-phase clouds, J. Atm. Sci., 64, 3372–3375, doi:10.1175/JAS4035.1, 2007.

Korolev, A. V. and Field, P. R.: Assessment of the performance of the inter-arrival time algorithm to identiy ice shattering artifacts in cloud particle probe measurements, Atm. Meas. Tech., 8, 761–777, 2015.

Korolev, A. V., Emery, E. F., Strapp, J. W., Cober, S. G., and Isaac, G. A.: Quantification of the effects of shattering on airborne ice particle measurements, J. Atm. Ocean. Tech., 30, 2527–2553, doi:10.1175/JTECH-D-13-00115.1, 2013a.

Korolev, A. V., Strapp, J. A., Isaac, G. A., and Emery, E.: Improved airborne hot-wire measurements of ice water content in clouds, J. Atm. Ocean. Tech., 30, 2121–2131, doi:10.1175/JTECH-D-13-00007.1, 2013b.

Lasher-Trapp, S., Leon, D. C., DeMott, P. J., Villanueva-Birriel, C. M., Johnson, A. V., Moser, D. H., Tully, C. S., and Wu, W.: A multisensor investigation of rime splintering in tropical maritime cumuli, J. Atm. Sci., 73, 2547–2564, doi:10.1175/JAS-D-15-0285.1, 2016.

Lau, K.-M. and Wu, H.-T.: Climatology and changes in tropical ocean rainfall characteristics inferred from Tropical Rainfall Measuring Mission (TRMM) data (1998-2009), J. Geophys. Res., 116, doi:10.1029/2011JD015827, 2011.

Lauber, A., Kiselev, A., Pander, T., Handmann, P., and Leisner, T.: Secondary ice formation during freezing of levitated droplets, J. Atm. Sci., doi:10.1175/JAS-D-18-0052.1, 2018.

Lawson, P., Gurganus, C., Woods, S., and Bruintjes, R.: Aircraft observations of cumulus microphysics ranging from the tropics to midlatitudes: Implications for a “new" secondary ice process, J. Atm. Sci., 74, 2899–2920, doi:10.1175/JAS-D-17-0033.1, 2017.

Lawson, R. P., Woods, S., and Morrison, H.: The microphysics of ice and precipitation development in tropical cumulus clouds, J. Atm. Sci., 72, 2429–2445, doi:10.1175/JAS-D-14-0274.1, 2015.

Leisner, T., Pander, T., Handmann, P., and Kiselev, A.: Secondary ice processes upon heterogeneous freezing of cloud droplets, 14th Conf. on Cloud Physics and Atmospheric Radiation, Amer. Meteor. Soc, Boston, MA, 2014.

Lohmann, U.: Anthropogenic aerosol influences on mixed-phase clouds, Curr. Clim. Change Rep., doi:10.1007/s40641-017-0059-9, 2017.

Mason, B. J. and Jonas, P. R.: Evolution of droplet spectra and large droplets by condensation in cumulus clouds, Q. J. Roy. Meteorol. Soc., pp. 23–38, 1974.

McFarquhar, G. M., Um, J., Freer, M., Baumgardner, D., Kok, G. L., and Mace, G.: Importance of small ice crystals to cirrus properties: Observations from Tropical Warm Pool International Cloud Experiment (TWP-ICE), Geophys. Res. Lett., 34, doi:10.1029/2007GL029865, 2007.

Milbrandt, J. A. and Morrison, H.: Parameterization of cloud microphysics based on the prediction of bulk ice particle properties. Part III: Introduction of multiple free categories, J. Atm. Sci., 73, 975–995, doi:10.1175/JAS-D-15-0204.1, 2015.

Möhler, O., Field, P. R., Connolly, P., Benz, S., Saathoff, H., Schnaiter, M., Wagner, R., Cotton, R., Krämer, M., Mangold, A., and Heymsfield, A. J.: Efficiency of the deposition mode ice nucleation on mineral dust particles, Atmos. Chem. Phys., 6, 3007–3021, doi:10.5194/acp-6-3007-2006, 2006.

Möhler, O., Georgakopoulos, D. G., Morris, C. E., Benz, S., Ebert, V., Hunsmann, S., Saathoff, H., Schnaiter, M., and Wagner, R.: Heterogeneous ice nucleation activity of bacteria: new laboratory experiments at simulated cloud conditions, Biogeosci., 5, 1425–1435, doi:10.5194/bg-5-1425-2008, 2008.

Morales-Betancourt, R., Lee, D., Oreopoulos, L., Sud, Y. C., Barahona, D., and Nenes, A.: Sensitivity of cirrus and mixed-phase clouds to the ice nuclei spectra in McRAS-AC: single column model simulations, Atmos. Chem. Phys., 12, 10 679–10 692, doi:10.5194/acp-12-10679-2012, 2012.

Morrison, H. and Milbrandt, J. A.: Parameterization of cloud microphysics based on the prediction of bulk ice particle properties. Part I: Scheme description and idealized tests, 72, 287–311, doi:10.1175/JAS-D-14-0065.1, 2015.

Morrison, H., shupe, M. D., Pinto, J. O., and Curry, J. A.: Possible roles of ice nucleation mode and ice nuclei depletion in the extended lifetime of Arctic mixed-phase clouds, Geophys. Res. Lett., 32, doi:10.1029/2005GL023614, 2005.

Mossop, S. C.: Production of secondary ice particles during the growth of graupel by riming, Q. J. Roy. Meteor. Soc., 102, 45–57, doi:10.1002/qj.49710243104, 1976.

Mossop, S. C.: Secondary ice particle production during rime growth: The effect of drop size distribution and rimer velocity, Q. J. R. Meteorol. Soc., 111, 1113–1124, doi:10.1002/qj.49711147012, 1985.

Mülmenstädt, J., Sourdeval, O., and Delano e, J.: Frequency of occurrencee of rain from liquid-, mixed-, and ice-phase clouds derived from A-Train satellite retrievals, Geophys. Res. Lett., 42, 6502–6509, doi:10.1002/2015GL064604, 2015.

O'Sullivan, D., Murray, B. J., Ross, J. F., Whale, T. F., Price, H. C., Atkinson, J. D., Umo, N. S., and Webb, M. E.: The relevance of nanoscale biological fragments for ice nucleation in clouds, Sci. Rep., 5, doi:10.1038/srep08082, 2015.

Otkin, J., Huang, H.-L., and Seifert, A.: A comparison of microphysical schemes in the WRF model during a severe weather event, 7th Annual WRF User's Workshop, Boulder, CO, 2006.

Paukert, M. and Hoose, C.: Modeling immersion freezing with aerosol-dependent prognostic ice nuclei in Arctic mixed-phase clouds, J. Geophys. Res., 119, 9073–9092, doi:10.1002/2014JD021917, 2014.

Paukert, M., Hoose, C., and Simmel, M.: Redistribution of ice nuclei between cloud and rain droplets: Parameterization and application to deep convective clouds, J. Adv. Mod. Earth Sys., 9, 514–535, doi:10.1002/2016MS000841, 2017.

Phillips, V., DeMott, P., and Andronache, C.: An empirical parameterization of heterogeneous ice nucleation for multiple chemical species of aerosol, J. Atmos. Sci., 65, 2757–2783, doi:10.1175/2007JAS2546.1, 2008.

Phillips, V. T. J., Blyth, A. M., Brown, P. R. A., Choularton, T. W., and Latham, J.: The glaciation of a cumulus cloud over New Mexico, Q. J. Roy. Meteorol. Soc., 127, 1513–1534, doi:10.1002/qj.49712757503.

Phillips, V. T. J., Yano, J.-I., Formenton, M., Ilotoviz, E., Kanawade, V., Kudzotsa, I., Sun, J., andA. G. Detwiler, A. B., Khain, A., and Tessendorf, S. A.: Ice multiplication by breakup in ice-ice collisions. Part II: Numerical simulations, J. Atm. Sci., 74, 2789–2811, doi:10.1175/JAS-D-16-0223.1, 2017a.

Phillips, V. T. J., Yano, J.-I., and Khain, A.: Ice multiplication by breakup in ice-ice collisions. Part I: Theoretical formulations, J. Atm. Sci., 74, 1705–1719, doi:10.1175/JAS-D-16-0224.1, 2017b.

Pieri, A. B., Hardenberg, J., Parodi, A., and Provenzale, A.: Sensitivity of precipitation statistics to resolution, microphysics, and convective parameterization: A case study with the high-resolution WRF climate model over Europe, J. Hydromet., 16, 1857–1872, doi:10.1175/JHM-D-15-0221.1, 2015.

Prein, A. F., Holland, G. J., Rasmussen, R. M., Done, J., Ikeda, K., Clark, M. P., and Liu, C. H.: Importance of regional climate model grid spacing for the simulation of heavy precipitation in the Colorado headwaters, J. Clim., 26, 4848–4857, doi:10.1175/JCLI-D-12-00727.1, 2013.

Rosenfeld, D. and Gutman, G.: Pollution and clouds, Physics World, 14, 259–283, 2001.

Segal, Y. and Khain, A.: Dependence of droplet concentration on aerosol conditions in different cloud types: Application to droplet concentration parameterization of aerosol conditions, J. Geophys. Res.-Atmos., 111, doi:10.1029/2005/JD006561, 2006.

Seifert, A.: Parametrisierung wolkenmikrophysikalischer Prozesse und Simulation konvektiver Mischwolken, Ph.D. thesis, Universität Karlsruhe, 2002.

Seifert, A. and Beheng, K. D.: A two-moment cloud microphysics parameterization for mixed-phase clouds. Part I: Model description, Meteorol. Atmos. Phys., 92, 45–66, doi:10.1002/2014JD021917, 2006.

Sud, Y. C. and Walker, G. W.: Influence of ice-phase physics of hydrometeors on moist-convection, Geophys. Res. Lett., 30, doi:10.1029/2003GL017587, 2003.

Sullivan, S., Hoose, C., and Nenes, A.: Investigating the contribution of secondary production to ice crystal number concentrations, J. Geophys. Res., doi:10.1002/2017JD026546, 2017.

Sullivan, S. C., Betancourt, R. M., Barahona, D., and Nenes, A.: Understanding cirrus ice crystal number variability for different heterogeneous ice nucleation spectra, Atmos. Chem. Phys., 16, 2611–2629, doi:10.5194/acp-16-2611-2016, 2016.

Sullivan, S. C., Kiselev, A., Leisner, T., Hoose, C., and Nenes, A.: Initiation of secondary ice production in clouds, Atmos. Chem. Phys., 18, 1593–1610, doi:10.5194/acp-18-1593-2018, 2018.

Takahashi, T., Nagao, Y., and Kushiyama, Y.: Possible high ice particle production during graupel-graupel collisions, J. Atmos. Sci., 52, 4523–4527, doi:10.1175/1520-0469, 1995.

Taylor, J. W., Choularton, T. W., Blyth, A. M., Liu, Z., Bower, K. N., Crosier, J., Gallagher, M. W., Williams, P. I., Dorsey, J. R., Flynn, M. J., Bennett, L. J., Huang, Y., French, J., Korolev, A., and Brown, P. R. A.: Observations of cloud microphysics and ice formation during COPE, Atmos. Chem. Phys., 16, doi:10.5194/acp-16-799-2016, 2016.

Thompson, G., Rasmussen, R. M., and Manning, K.: Explicit forecasts of winter precipitation using an improved bulk microphysics scheme. Part I: Description and sensitivity analysis, Mon. Weath. Rev., 132, 519–542, doi:10.1175/1520-0493(2004)132>0519:EFOWPU<2.0.CO;2, 2004.

Tiedtke, M.: A comprehensive mass flux scheme for cumulus parameterization in large-scale models, Mon. Weath. Rev., 117, 1779–1800, doi:10.1175/1520-0493(1989)117>1779:ACMFSF<2.0.CO;2, 1989.

Vardiman, L.: The generation of secondary ice particles in clouds by crystal-crystal collision, J. Atmos. Sci., 35, 2168–2180, doi:10.1175/1520-0469, 1978.

Viale, M., Houze, R. A., and Rasmussen, K. L.: Upstream orographic enhancement of a narrow cold-frontal rainband approaching the Andes, Mon. Weather Review, 141, 1708–1730, doi:10.1175/MWR-D-12-00138.1, 2013.

Wildeman, S., Sterl, S., Sun, C., and Lohse, D.: Fast dynamics of water droplets freezing from the outside in, Phys. Rev. Lett., 118, doi:10.1103/PhysRevLett.118.084101, 2017.

Willison, J., Robinson, W. A., and Lackmann, G. M.: The importance of resolving mesoscale latent heating in the North Atlantic storm track, J. Atmos. Sci., 70, 2234–2250, doi:10.1175/JAS-D-12-0226.1, 2013.

Wisner, C., Orville, H. D., and Myers, C.: A numerical model of a hail-bearing cloud, J. Atm. Sci., 29, 1160–1181, doi:10.1175/1520-0469(1972)029>1160% 3AANMOAH<2.0.CO% 3B2, 1972.

Yang, Q., Leung, L. R., Rauscher, S. A., Ringler, T. D., and Taylor, M. A.: Atmospheric moisture budget and spatial resolution dependence of precipitation extremes in aquaplanet simulations, J. Clim., 27, 3565–3581, doi:10.1175/JCLI-D-13-00468.1, 2014.

Yano, J.-I. and Phillips, V. T. J.: Ice-ice collisions: an ice multiplication process in atmospheric clouds, J. Atmos. Sci., 68, 322–333, doi:10.1175/2010JAS3607.1, 2011.

Yano, J.-I., Phillips, V. T. J., and Kanawade, V.: Explosive ice multiplication by mechanical break-up in ice-ice collisions: a dynamical system-based study, Q. J. Roy. Meteorol. Soc., 142, 867–879, doi:10.1002/qj.2687, 2016.

Zhu, H., Maloney, E., Hendon, H., and Stratton, R.: Effects of the changing heating profile associated with melting layers in a climate model, Q. J. Roy. Meteorol. Soc., doi:10.1002/qj.3166, 2017.